

# Journal of Geophysical Research: Oceans

## RESEARCH ARTICLE

10.1002/2016JC012362

**Key Points:**

- Net cross-shore transport results from the combination of three transport mechanisms that turn on and off in response to the forcing conditions
- Barotropic transport at depth during storms results in net offshore transport. Baroclinic transport at depth during stratified periods results in onshore transport
- Tidal plume fronts manifest as strong pulses of seaward transport at depth, presenting a dynamical component not observed in the far-field

**Correspondence to:**

R. P. Flores,  
rfloresa@uw.edu

**Citation:**

Flores, R. P., S. Rijsburger, A. R. Horner-Devine, A. J. Souza, and J. D. Pietrzak (2017), The impact of storms and stratification on sediment transport in the Rhine region of freshwater influence, *J. Geophys. Res. Oceans*, 122, 4456–4477, doi:10.1002/2016JC012362.

Received 22 SEP 2016

Accepted 20 MAR 2017

Accepted article online 23 MAR 2017

Published online 31 MAY 2017

## The impact of storms and stratification on sediment transport in the Rhine region of freshwater influence

Raúl P. Flores<sup>1,2</sup> , Sabine Rijsburger<sup>3</sup> , Alexander R. Horner-Devine<sup>1</sup> , Alejandro J. Souza<sup>4</sup> , and Julie D. Pietrzak<sup>3</sup>

<sup>1</sup>Department of Civil and Environmental Engineering, University of Washington, Seattle, Washington, USA,

<sup>2</sup>Departamento de Obras Civiles, Universidad Técnica Federico Santa María, Valparaíso, Chile, <sup>3</sup>Department of Hydraulic Engineering, Delft University of Technology, Delft, Netherlands, <sup>4</sup>National Oceanography Centre, Liverpool, UK

**Abstract** We present measurements of along and across-shore sediment transport in a region of the Dutch coast 10 km north of the Rhine River mouth. This section of the coast is characterized by strong vertical density stratification because it is within the midfield region of the Rhine region of freshwater influence, where processes typical of the far-field, such as tidal straining, are modified by the passage of distinct freshwater lenses at the surface. The experiment captured two storms, and a wide range of wind, wave, tidal and stratification conditions. We focus primarily on the mechanisms leading to cross-shore sediment flux at a mooring location in 12 m of water, which are responsible for the exchange of sediment between the nearshore and the inner shelf. Net transport during storms was directed offshore and influenced by cross-shelf winds, while net transport during spring tides was determined by the mean state of stratification. Tidal straining dominated during neap tides; however, cross-shore transport was negligible due to small sediment concentrations. The passage of freshwater lenses manifested as strong pulses of offshore transport primarily during spring tides. We observe that both barotropic and baroclinic processes are relevant for cross-shore transport at depth and, since transport rates due to these competing processes were similar, the net transport direction will be determined by the frequency and sequencing of these modes of transport. Based on our observations, we find that wind and wave-driven transport during storms tends move fine sediment offshore, while calmer, more stratified conditions move it back onshore.

**Plain Language Summary** This paper describes different mechanisms capable of exchanging sediments, contaminants and biological materials between shallow areas close to the shore and deep offshore areas, in a coastal region influenced by the freshwater discharge of a large river. In general, our results show that storms, with high winds and waves, move sediment offshore whereas calmer periods when the water column is stratified move sediment onshore. The total balance is defined by the frequency and sequencing of these modes of transport.

### 1. Introduction

Rivers deliver significant amounts of freshwater and sediment to the ocean [Dagg *et al.*, 2004; Milliman and Syvitski, 1992], creating buoyant plumes that become the interface between estuaries and continental shelf seas. Upon exiting the estuary, the influence of Earth's rotation eventually turns riverine freshwater anticyclonically (to the right in the Northern hemisphere), establishing a narrow current that can flow tens of kilometers along the coast [Fong and Geyer, 2001, 2002; Pietrzak *et al.*, 2002; Horner-Devine *et al.*, 2015]. Consequently, river plumes are critical in determining the advection, dispersion, and redistribution of sediments, pollutants, and biota, thus controlling primary productivity and several other environmental issues in coastal regions.

Circulation dynamics in river plumes are largely baroclinic and vary significantly according to riverine freshwater discharge, tidal amplitude, coastline geometry, ocean currents, wind stress, and the effect of Earth's rotation [Horner-Devine *et al.*, 2015]. In shallow tidal systems, such as the Rhine [Simpson, 1997] or Liverpool Bay [Verspecht *et al.*, 2009, 2010], bottom friction is also relevant by setting the cross-shore extension of the plume and the scale of the bottom boundary layer, which can often influence a large portion of the water

column. These systems are often referred to as Regions of Freshwater Influence (ROFIs). In these systems, tidal current structure and the vertical distribution of SPM (Suspended Particulate Matter) respond directly to the onset and destruction of stratification, which in turn is determined by the interaction between the freshwater plume and tidal, wind, and wave-mixing processes [Simpson and Souza, 1995; Visser *et al.*, 1994; Joordens *et al.*, 2001; Peperzak *et al.*, 2003].

The outflow discharge from the Rhine river into the shallow and highly energetic coastal areas of the Southern North Sea sustains a large ROFI, that extends for over 100 km along the Dutch coast and, on average, remains concentrated within a 20 km-wide coastal strip [De Kok, 1996; Pietrzak *et al.*, 2011]. Three main dynamical regions can be distinguished [Garvine, 1984; Hetland, 2005; Horner-Devine *et al.*, 2009, 2015]: the near-field, where the momentum of the plume layer dominates over its buoyancy, the midfield, where Earth's rotation begins to dominate and turns the plume in the down coast direction, and the far-field, where a buoyant density current has been established flowing parallel to the coast toward the northeast. Physical processes leading to the switching of stratification, the modification of tidal currents, and midshelf sediment accumulation have been extensively studied in the far-field [Simpson and Souza, 1995; van der Hout *et al.*, 2015; De Boer *et al.*, 2006; Rijnsburger *et al.*, 2016], where cross-shore tidal straining [Simpson *et al.*, 1990] plays a key role. Closer to the river mouth, in the midfield region, the tidal advection of freshwater lenses strongly modifies stratification and current patterns from those observed in the far-field [Van Alphen *et al.*, 1988; Horner-Devine *et al.*, 2017], with effects on transport processes that have not yet been fully investigated.

The potential impact of river plume processes on SPM transport dynamics has gained much relevance over the last few decades, especially in light of the pressure that large-scale engineering projects have exerted on the morphodynamics of coastal areas. For the particular case of the Dutch coast, the completion of the Sand Engine [Stive *et al.*, 2013; de Schipper *et al.*, 2016] in 2011 and the construction of an extension of the Port of Rotterdam have introduced modifications to the morphology of the coastline and nearshore SPM transport patterns. The Sand Engine is a 21.5 million m<sup>3</sup> sand nourishment located 10 km north of the Rhine River mouth, built to protect the beaches and dunes along the Dutch coast from erosion and provide a defence to flooding of the low-lying lands of The Netherlands [Stive *et al.*, 2013].

SPM regimes in river plumes are different from those of wave-dominated environments in the nearshore and those of shelf seas. Stratification leads to the suppression of turbulence at the pycnocline [Geyer, 1993; de Nijs *et al.*, 2010], trapping suspended matter below it. The continuous change between stratified and well-mixed conditions in shallow river plumes, such as the Rhine, complicates the task of inferring subsurface SPM fluxes from remote sensing data or surface measurements [Pietrzak *et al.*, 2011; van der Hout *et al.*, 2015]. Geyer *et al.* [2004] concluded that sediment transport in river-influenced regions is often dominated by near-bottom fluxes, which suggests that near-bed measurements are required to avoid erroneous conclusions about the magnitude and direction of transport.

In this study, we will present field measurements taken 1 km offshore and 10 km north from the Rhine River mouth (in the vicinity of the Sand Engine) in order to investigate the sediment fluxes in a shallow midfield plume region, a region strongly influenced by the propagation of tidally generated freshwater lenses as well as processes characteristic of the far-field. We give a global description of sediment dynamics in the inner shelf region of the ROFI and their response to storms (barotropic) and stratified (baroclinic) periods. The analysis is focused on the identification of the underlying physical mechanisms that determine the direction and intensity of sediment transport, emphasizing near-bottom dynamics that are dominated by higher concentrations and larger particle sizes relevant for coastal morphodynamics. The paper is organized as follows: Section 2 gives an overview of previous work that is relevant for the analysis we present in this study. Section 3 describes the measurements, conditions, and methods. Density, current structure, suspended sediment concentrations, and results for the suspended sediment fluxes are presented in section 4. Section 5 presents a discussion of the findings and the role of stratification on transport processes in the midfield region of the Rhine ROFI, and section 6 presents the conclusions.

## 2. Background

Processes leading to SPM transport in the Rhine ROFI are strongly tied to density stratification patterns [van der Hout *et al.*, 2015; Joordens *et al.*, 2001]. Variations in stability of the Rhine ROFI occur at different

timescales [Simpson *et al.*, 1993; Simpson, 1997]. The fortnightly cycle of the tides imposes a predictable variation in the tidal-mixing component, which is reflected in a neap-spring time-scale variation in stratification. Superimposed on tidal processes, the variability in wind and wave forcing, along with a time-dependent river discharge often produce sources of stratification variability in a much shorter timescale.

Observations in the far-field of the Rhine ROFI (40–80 km from the river mouth) show a semidiurnal variation during periods of stratification [Simpson *et al.*, 1993; Simpson and Souza, 1995]. In this region of the North Sea, the tide is dominated by the M2 semidiurnal component and is well described by a progressive Kelvin wave traveling to the northeast, with tidal velocities in phase with tidal elevation. Tidal straining results from the interaction of the tidal shear with the horizontal density gradients, alternately inducing and destroying stratification at the tidal frequency [Simpson *et al.*, 1990]. Stratification develops during the flood, reaching its maximum at local high water [De Boer *et al.*, 2006]. The process is reversed during the ebb tide, such that minimum stratification occurs at low water. Strain-induced stratification requires the occurrence of strong cross-shore exchange currents, which cannot come from the barotropic tidal currents that tend to be parallel to the coast. The generation of strong cross-shore currents is explained by the modification of tidal ellipses due to the effect of stratification [Visser *et al.*, 1994; Verspecht *et al.*, 2010]. Tidal current vectors show elliptical trajectories in the horizontal plane, and can be decomposed in two counterrotating phasors [Prandle, 1982]. Following Ekman dynamics, the one that rotates opposite to Earth's rotation has a much greater boundary layer thickness than the component that rotates in the same direction as the Earth. The onset of stratification decouples the water column at the pycnocline by reducing the eddy viscosity [Visser *et al.*, 1994], and the upper layer is free to move under the barotropic forcing. This increases the amplitude of clockwise (anticyclonic) currents at the surface with respect to the unstratified case. Due to the proximity of the coast, near-bottom currents become more cyclonic such that at any time the depth-averaged cross-shore velocity is zero because of continuity constraints [De Boer *et al.*, 2006]. This combined effect creates a strongly sheared cross-shore flow, with cross-shore currents that show 180° phase difference between the surface and bottom, and maximum stratification is achieved at times of the maximum relative displacement between the lower and upper layers. Simpson and Souza [1995] first realized the two-way interaction between the cross-shore density gradients and semidiurnal counterrotating currents in the Rhine ROFI.

In this work, we refer to tidal straining as the generation of counterrotating tidal ellipses by vertical stratification, resulting in the cross-shore tilting of the isopycnals [Visser *et al.*, 1994; Simpson and Souza, 1995]. In the Rhine ROFI, there are several other straining mechanisms that contribute to the generation of stratification and transport processes, which are described in detail in De Boer *et al.* [2008]. Our definition of tidal straining corresponds to the term  $S_x$  in De Boer *et al.* [2008] and Rijnsburger *et al.* [2016].

In the absence of stratification (barotropic conditions), Earth's rotation induces small ellipticities that result in cross-shore currents during both neap and spring tides [De Boer *et al.*, 2006]. It is important to note that these cross-shore currents are just a small fraction of the dominant alongshore velocities, but still allow for cross-shore exchange during energetic storm periods with strong wind and wave mixing.

Closer to the river mouth, additional processes generate different stratification and current patterns from those observed in the far-field [Van Alphen *et al.*, 1988; De Boer *et al.*, 2008]. The discharge of the Rhine River is strongly modulated by the semidiurnal tidal wave propagating into the estuary. Consequently, freshwater enters the coastal zone as a series of periodic pulses released during ebb tide [de Ruijter *et al.*, 1997] generating strong fronts on their boundaries that are similar to tidal plume fronts observed in other systems, such as the Connecticut [Garvine, 1974, 1977] and Columbia [Horner-Devine *et al.*, 2009] River plumes. Freshwater lenses have been observed to propagate northeastward along the Dutch coast at velocities up to 0.5  $\text{ms}^{-1}$ , while undergoing strong mixing and deformation before being incorporated to the plume [de Ruijter *et al.*, 1997]. Fronts have also been observed to propagate all the way to the beach generating rapid current responses in the lower layer [Horner-Devine *et al.*, 2017], in addition to strong density gradients in time and space.

In the midfield region, the frontal processes characteristic to the near-field and the tidal straining processes characteristic of the far-field interact, as shown by De Boer *et al.* [2008]. Moreover, the counterrotating velocity field generated by tidal straining results in the onshore and offshore advection of the entire ROFI, generating a periodic front that is displaced by over 7 km each tidal cycle [Simpson and Souza, 1995] that

interacts with the ejected freshwater lenses. This interaction likely results in asymmetric processes driven by the timing of the freshwater lenses, with the potential of impacting cross-shore exchange.

Cross-shore circulation patterns and associated transport processes are also influenced by wind forcing, especially during storms. In recent years, cross-shelf winds have been shown to generate cross-shore exchange flows aligned with the wind stress in shallow inner shelf regions where the surface and bottom boundary layers overlap [Lentz, 1995; Lentz and Fewings, 2012]. Fewings *et al.* [2008] demonstrated that alongshore winds at a location in 12 m of water do not drive substantial cross-shelf circulation (as opposed to the mid and outer shelf) and that circulation is driven by the cross-shelf wind, wave forcing, and tides. Wind stress has also been shown to be one of the dominant terms in the depth-averaged momentum balance at depths less than 30 m [Fewings and Lentz, 2010; Gutierrez *et al.*, 2006], where it balances the pressure gradient (coastal setup or setdown) induced mainly by the cross-shore winds.

Many investigations in the Rhine ROFI have shown the effects of haline stratification on the vertical distribution of sediment [Pietrzak *et al.*, 2011; van der Hout *et al.*, 2015] and the sinking rates of chlorophyll and phytoplankton [Peperzak *et al.*, 2003; Joordens *et al.*, 2001]. Pietrzak *et al.* [2011] showed that high SPM values can be observed near the surface over the full extension of the plume when the Rhine ROFI is well-mixed in the vertical, whereas during stratified periods SPM is not visible in the near-surface layer as it gets trapped below the pycnocline. This was also reported by Joordens *et al.* [2001] and more recently by van der Hout *et al.* [2015], using cross-shore transects at different locations along the Dutch coast.

In situ SPM transport studies in the Rhine ROFI have been mostly conducted at distances greater than 40 km from the estuary mouth in the far-field plume [McCandliss *et al.*, 2002; Van Alphen, 1990; van der Hout *et al.*, 2015]. At a study site located 80 km north of the river mouth, van der Hout *et al.* [2015] reported that the accumulation of SPM in the cross-shore direction over a year is a significant percentage of the yearly residual alongshore transport, leading to a persistent midshelf turbidity maximum zone with peak concentrations located 1.25–1.5 km from the coast. Furthermore, they suggest that the nearshore presence of turbidity maximum is strongly influenced by processes related to stratified plume dynamics, such as asymmetry in cross-shore straining.

In one of the few in situ SPM studies located in the midfield region, Horner-Devine *et al.* [2017] described a new cross-shore exchange mechanism in which the tidally generated front from the Rhine River outflow propagates onshore and drives suspended sediment from the surfzone 2–3 km offshore. This mechanism involves the interaction between nearshore wave-induced sediment resuspension and plume-generated pulses of seaward velocity in the lower layer due to the onshore propagation of the front near the surface. In their study, Horner-Devine *et al.* [2017] found that suspended sediment transport measured at a mooring located at 12 m depth and 10 km north of the Rhine River mouth was strongly dominated by pulses of seaward transport that were timed with the passage of the tidal plume front. Based on the timing of elevated SSC relative to the front, low bed stresses and high cross-shore velocities, they conclude that the transport pulses are the result of advection from the surf zone region rather than local resuspension. This new mechanism provides a link between the shoreline and offshore coastal waters through the interaction of baroclinic river plume processes and surfzone wave activity. Transport due to frontal pumping dominated the cross-shore flux during the 2013 experiment and this process is also observed in the data from the 2014 experiment presented here (see our Figure 9). One of the objectives of the present study is to determine whether this mechanism dominates transport dynamics close to the river mouth under a different set of forcing conditions.

### 3. Setup and Methods

#### 3.1. Measurements

Field observations were carried out from 15 September to 28 October (year days 258–301), 2014, comprising almost two complete neap-spring cycles. These measurements are part of a large scientific field campaign called STRAINS (Stratification Impacts on Nearshore Sediment Transport), which focused on the role of ROFI processes and stratification on sediment transport near the Sand Engine and their implications along the Dutch coast. Two moorings were deployed approximately 10 km north-east of the mouth of the Rotterdam waterway at nominal depths of 12 and 18 m, corresponding to 1.5 and 6 km from the coast, respectively (Figure 1a).

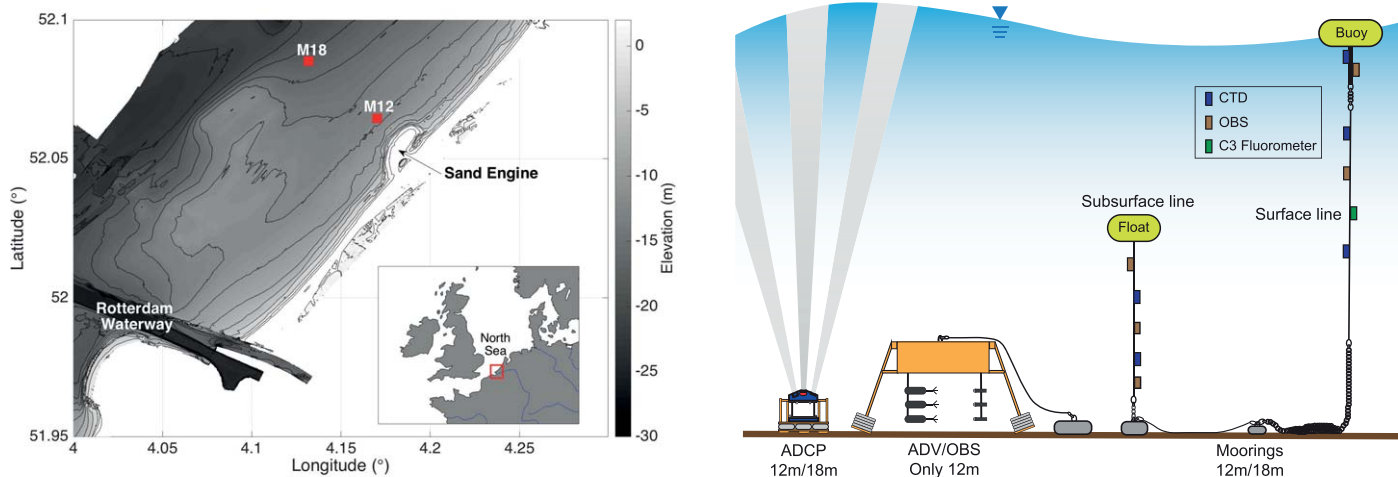


**Figure 1.** Study area and moorings. (left) Dutch coast near the Rhine river mouth. Red squares mark the location of moorings and bottom frames at 12 and 18 m depth. (right) Instrumentation schematics. Moorings at each site were spaced by 50 m.

The moorings were located in the midfield region of the Rhine ROFI, i.e., within the excursion of the tidal plume front generated by the freshwater outflow from the Rhine. The moorings were designed to measure vertical profiles of conductivity, temperature, pressure, and suspended sediment concentration throughout the water column using arrays of CTDs (Conductivity-Temperature-Depth) and OBS (optical backscatter) sensors, from which salinity and density profiles were derived. Five CTDs (Seabird) and five OBSs were placed at the 12 m mooring, whereas four CTDs and five OBSs were placed at 18 m depth, providing a detailed description of both salinity and sediment concentrations throughout the tidal cycle. A schematic of the 12 m mooring is shown in Figure 1b. Sampling periods were typically 30 s, but ranged between 20 and 50 s depending on the instrument. OBS sensors were intercalibrated using formazine solutions prior to deployment in the laboratory in order to account for sensor sensitivity and the data were converted to mass concentrations using a conversion based on over 400 bottle samples collected by the Port of Rotterdam in this region of the Dutch coast.

Vertical profiles of current speed were measured at each location using a bottom-mounted four beam Acoustic Doppler Current Profiler (ADCP; 1200 kHz RDI WorkHorse), sampling at 1 Hz, with the first bin centered approximately 1.5 m above the seabed and vertical resolution of 0.25 m (bin size). The raw data were averaged into 10 min blocks to obtain mean current profiles, and the N-E velocity components were rotated to alongshore and cross-shore components using the inclination of the major axis of the tidal ellipses, which resulted in a rotation angle of 42.5° from the North. Alongshore velocities are positive toward the northeast and cross-shore velocities are positive in the offshore direction. The harmonic analysis done to obtain tidal ellipses was performed using the T-TIDE code [Pawlowicz et al., 2002].

Hydrodynamic flow conditions were complemented with the measurement of 3-D near-bottom dynamics and turbulence at the 12 m site, using three synchronized 6 MHz Sontek Acoustic Doppler Velocimeters (ADV), sampling at 16 Hz and mounted on a frame 0.25, 0.5, and 0.75 m above the bottom, respectively. The ADVs were mounted on an arm away from the frame to avoid turbulent perturbations due to the frame itself. The raw ADV data were quality controlled and despiked using the three-dimensional phase space algorithm of Goring and Nikora [2002]. Near-bottom mean tidal velocities were estimated by time averaging over a 10 min period, and turbulent velocity components  $u'$ ,  $v'$ , and  $w'$  were obtained by removing the tidal trend. The mean and the turbulent horizontal velocity components were rotated to alongshore and cross-shore components, using the same procedure as with the ADCP velocities. Collocated fast sampling OBSs were also deployed and synchronized with the ADVs to measure near-bottom concentrations and fluxes (Figure 1b).

### 3.2. Conditions

Figure 2 shows the forcing conditions observed during the deployment. The Rhine River discharge ranged from approximately 500 to 2500  $\text{m}^3\text{s}^{-1}$ , with a mean value of 1500  $\text{m}^3\text{s}^{-1}$ , which corresponds to a 60% of

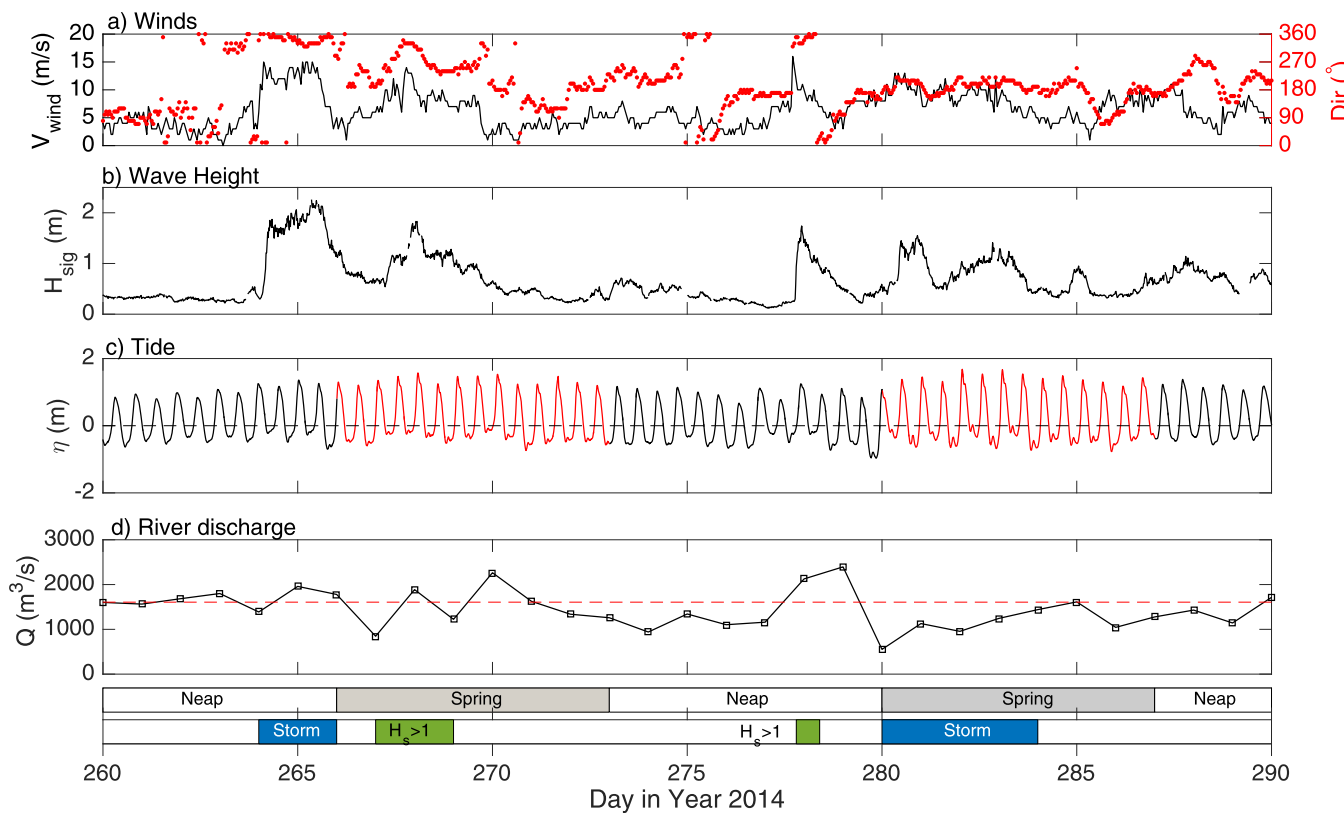


**Figure 2.** Conditions. (a) Wind speed (solid black line) and wind direction (solid gray line). Meteorological convention is followed. (b) Significant wave height from Waverider buoy. (c) Tidal elevation measured at Scheveningen station. Colors indicate neap (black) and spring (red) tide. (d) Rhine River discharge. Dashed red line represents the average discharge for the study period. Bars indicate spring/neap periods and the occurrence of storms and  $H_{\text{sig}} > 1$  m.

the annual mean. The mean wind intensity was approximately  $6.4 \text{ ms}^{-1}$ , but variability was high in both magnitude and direction throughout the experiment. At the start of the deployment wind speeds were low ( $5 \text{ ms}^{-1}$ ), predominantly from the east. Winds intensified significantly during the first storm from days 264 to 266, reaching peak speeds of nearly  $15 \text{ ms}^{-1}$  persistently from the north. Toward the middle of the experiment winds decreased and ranged between  $3$  and  $7 \text{ ms}^{-1}$ , but an acute peak of  $17 \text{ ms}^{-1}$  was observed on day 278. Southerly winds on the order of  $10 \text{ ms}^{-1}$  were persistently observed during the second storm on days 280–284.

Wave statistics were measured with a Waverider buoy located 1 km to the southwest of the 12 m mooring. Significant wave heights followed winds closely, remaining less than 1 m for almost half of the deployment but peaking at nearly 2.5 m during the first storm and 1.5 m during the second storm (Figure 2b). Differences in wave heights between storms are attributed to wind direction; for the first storm winds were blowing from the north with a much greater fetch. Wave periods were generally less than 4 s, but peaked at almost 6 s during storms.

Tides in the vicinity of the Rhine ROFI are semidiurnal with amplitudes in the range of 1–2 m. During neap tides (see black periods on Figure 2c), the maximum tidal range was 1.6 m, whereas during spring tides (red periods Figure 2c) the maximum tidal range was 2.3 m.

### 3.3. Calculation of Friction Velocities and Sediment Fluxes

Reynolds stresses  $\overline{u'w'}$  and  $\overline{v'w'}$  can be estimated directly from the time-averaged correlations in turbulent velocity components, using the covariance method [Kim et al., 2000]. Provided the turbulence measurements are located within the bottom boundary layer, bottom stresses can be obtained as  $\tau_b = \rho (\overline{u'w'}^2 + \overline{v'w'}^2)^{1/2}$ , where  $\rho$  is the density of seawater.

The separation of shear stresses exerted on the bed by the tidal currents and wave motion is a necessary step to investigate the dynamics of sediment resuspension in shallow depths subjected to wave forcing. As

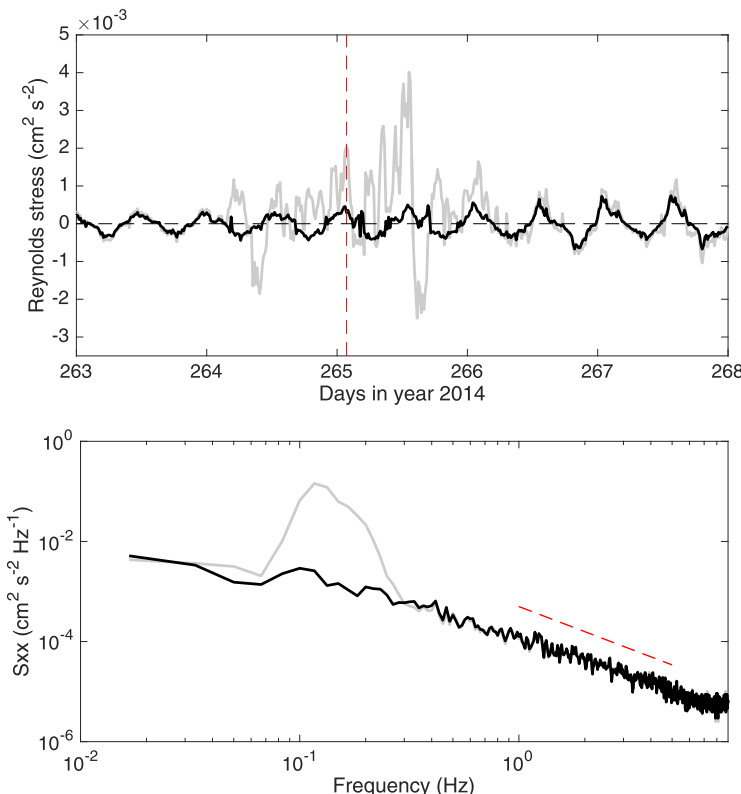


**Figure 3.** Wave-turbulence decomposition. (a) Turbulent stresses after wave removal (black line) and covariance of combined wave and turbulent velocities (gray line). (b) Spectral density for the  $x$  velocity component before and after wave removal (gray and black lines, respectively). Red-dashed line indicates the  $-5/3$  slope. The time of the burst for which spectrum is shown is indicated by the red vertical line in Figure 3a.

noted in Figure 2, wave heights up to 2.5 m were observed during storm periods, which would certainly make bottom shear stresses estimates unreliable since wave motions likely penetrate all the way to the seabed. To reduce the wave-induced bias on the Reynolds stresses, we use the linear filtration technique proposed by *Shaw and Trowbridge* [2001], which relies on two ADVs separated by a vertical distance larger than the length scale of the turbulent eddies (which scale with the vertical distance from the bottom) but smaller than the correlation scale of wave motion. Here, we have used a vertical separation between instruments of  $\Delta z = 0.5$  m using our lowest and highest ADVs. Figure 3a shows the covariance of turbulent velocity components and the Reynolds stresses after the removal of wave contamination, for a period centered around the first storm. Both estimates give very similar values when wave activity is low, but differ considerably during energetic conditions when wave-induced turbulence is significant. Frequency spectra for one burst are shown as an example of the turbulence decomposition method in Figure 3b. For this burst, indicated by the vertical line in Figure 3a, the influence of wave motions is significant in the range from 0.07 to 0.3 Hz. Agreement with the  $-5/3$  slope characteristic of the inertial subrange for frequencies above 1 Hz confirms that the instruments are resolving turbulence over a decade of frequencies in the inertial subrange, even in the presence of large waves. Bottom shear stresses due to current-induced turbulence were estimated from the wave-filtered Reynolds stresses, and the current friction velocity was calculated as  $u_{*c} = \sqrt{\tau_b / \rho}$ .

Representative wave parameters at our 12 m site were computed using the high-frequency ADV velocity measurements. Representative bottom orbital velocity ( $u_{br}$ ) and the representative wave frequency associated to  $u_{br}$  were obtained from the frequency spectra of horizontal velocities, following *Madsen* [1994] and *Wiberg and Sherwood* [2008]. Maximum wave-induced stresses at the bed are commonly parametrized in terms  $u_{br}$  and a wave friction factor  $f_w$  as  $\tau_{bw} = \frac{1}{2} \rho f_w u_{br}^2$ . In field conditions, we expect to have a hydraulically rough bed due to the presence of bed forms and sediment transport processes, particularly if the bed is sandy and exposed to waves capable of moving sediment. Therefore, we expect the wave friction factor to

fall within the rough turbulent regime such that  $f_w$  is only a function of the relative roughness parameter,  $f_w = f(k/a_b)$ , where  $k$  is the bed roughness and  $a_b$  is the maximum wave orbital excursion. Bed roughness is hard to measure in the field and is usually estimated indirectly using the particle size of bottom sediment. The wave friction factor is computed by  $f_w = \exp(5.213(k/a_b)^{0.194} - 5.977)$  [Swart, 1974], which is a commonly used parametrization for hydraulically rough flows in mobile beds. In the absence of bed form information, bed roughness was taken as  $k = 2d_{50}$  (obtained from samples of bed sediment) and orbital excursion is computed as  $a_b = u_{bw}/\omega$ , where  $\omega$  is the wave frequency. Wave friction velocity is obtained as  $u_{*w} = \sqrt{\tau_{bw}/\rho}$ .

Suspended sediment fluxes are computed directly from observations. Near-bottom sediment fluxes are computed using the three synchronized ADV and OBS measurements available from the bottom frame, which are averaged to obtain a representative value for the near-bottom suspended sediment fluxes. Near-surface fluxes were computed using a 1 m averaged velocity window (ADCP data) around the OBS sensor, placed in the surface line of the mooring (4 m below surface). Total fluxes, i.e., top to bottom, were computed by interpolating the OBS measurements onto the ADCP velocity grid. This calculation was not sensitive to the interpolation method, and linear interpolation between sensors was used.

## 4. Results

### 4.1. Density and Current Structure

The vertical and cross-shore structure of the observed density and velocity fields were highly variable during the observational campaign (Figure 4). Here we summarize the observed variability, focusing specifically on the relative influence of tidal straining, stratification, storms, and fronts on sediment transport. A more detailed description of the physical processes that dictate the plume behavior during this period will be described in subsequent work.

The beginning of the observational record (days 260–264) coincided with neap tides and low wind and wave mixing, which allowed the development of persistent and periodic stratification. The maximum top-bottom salinity difference was 8 psu and the mean was 3.5 psu, while maximum near-bottom currents were on the order of  $0.3 \text{ ms}^{-1}$  during flood tide. Tidal mixing is never sufficient to destroy stratification during these low-energy conditions, and the counterrotating tidal straining velocity field is evident in the highly sheared cross-shore current structure (Figure 4c). The signature of the plume front is observed as a sudden drop in surface density, associated with onshore surface velocities. Similar behavior is observed during the second neap tide period (days 273–280), where winds and waves remained less than  $5 \text{ ms}^{-1}$  and 1 m, respectively. Cross-shore current structure is dominated by onshore currents near the bottom, whereas offshore currents occur persistently in the top layer (except when the front is passing over the mooring). Depth-averaged alongshore currents during neap tides were on the order of  $0.4\text{--}0.6 \text{ ms}^{-1}$ .

Our observations show that storms can effectively eliminate vertical stratification in this midfield plume region. A big storm is observed during days 264–266, where wind speeds on the order of  $15 \text{ ms}^{-1}$  from the north and wave heights greater than 2 m (Figure 2) resulted in the complete homogenization of the water column (Figure 4a). The state of local vertical mixing at our 12 m site is primarily set by the combination of direct wind mixing and the offshore advection of the entire plume due to Ekman transport. During this event, cross-shore velocities are severely reduced as the effect of stratification on the velocity field is suppressed and currents become unidirectional throughout the water column (Figures 4b and 4c). Similar effects were observed during the second storm (days 280–284), however, lower wind speeds and wave heights (Figure 2a) allowed for weak stratification in the top-layer (1–3 m) at certain times.

The current and density structure during spring tides with weak to moderate wind forcing (less than  $8 \text{ ms}^{-1}$ ) responded differently according to wind direction. During spring tide days 267–270, the winds are downwelling favorable, which shifts the freshwater toward the coast. This shift is evident in the daily averaged salinities (not shown), which are lower during this period than any other time in the observational period and also a maximum in the cross-shore density difference. This period is also marked by strong fronts, which might be strengthened by the onshore wind forcing. Under these conditions, surface currents were persistently directed offshore while bottom currents are directed toward the coast, similar to a classic density-driven circulation profile (Figure 4c). This cross-shore flow structure has been previously observed in the Rhine ROFI by Souza and Simpson [1997] and

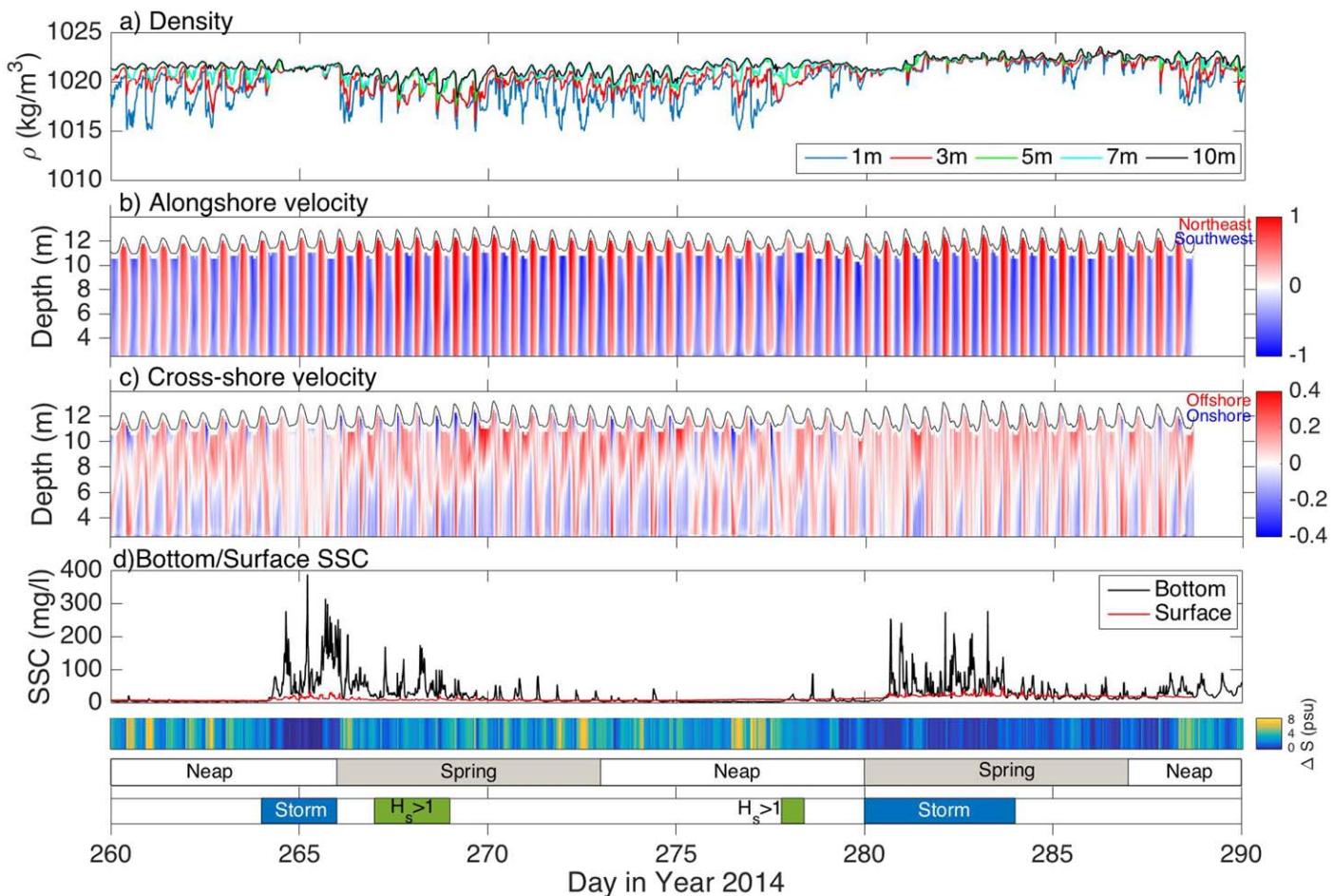


**Figure 4.** Density, current structure, and SSC at 12 m mooring. (a) Density. (b) Alongshore velocity ( $\text{ms}^{-1}$ ). (c) Cross-shore velocity ( $\text{ms}^{-1}$ ) (d) Near-bottom (black line) and near-surface (red line) suspended sediment concentration. Bottom bars show vertical stratification in terms of top-bottom salinity difference  $\Delta S$  (psu), neap/spring, and storm periods, and the occurrence of  $H_{\text{sig}} > 1$  (m).

Souza et al. [1997] in response to large horizontal density gradients. The signature of the tidal plume front was still strong in both density and velocity fields, with strong offshore current pulses at depth observed in response to a fast moving front with onshore surface velocities (Figures 4a and 4c). On the other hand, wind magnitude and direction during spring days 284–287 (see Figure 2a) were highly variable and allowed for both mixed and stratified periods. The relaxation of winds during day 284 resulted in an immediate onset of stratification, whereas stronger winds favoring the offshore or northeastward movement of the plume during days 285–287 led to more a vertically mixed state with freshwater observed only in the top CTD sensor. However, forcing was not strong enough to eliminate the presence of fronts at our site. Under these conditions, offshore currents seem to dominate cross-shore current structure, particularly in the top layer (Figure 4c). Maximum depth-averaged alongshore currents were on the order of  $1 \text{ ms}^{-1}$  for both spring tide periods.

#### 4.2. Suspended Sediment Concentrations and Fluxes

Sediment concentrations were highly variable during the study period and reveal the importance of wave forcing in sediment resuspension in this shallow ROFI region. We observe peak near-bottom concentrations on the order of  $400 \text{ mg L}^{-1}$  during storms (Figure 4d); however, significantly lower peak near-bottom concentrations around  $80 \text{ mg L}^{-1}$  during spring tides and  $40 \text{ mg L}^{-1}$  during neap tides were observed during calm periods with wave heights less than 1 m. The influence of large waves on sediment resuspension is examined by comparing SSC and wave and current friction velocities (Figure 5). No correlation between near-bottom suspended sediment concentration and tidal friction velocity  $u_{*c}^2$  is observed when the complete data set is used (Figure 5a), whereas for wavy periods ( $u_{br} > 5 \text{ cm s}^{-1}$ ), when the greatest

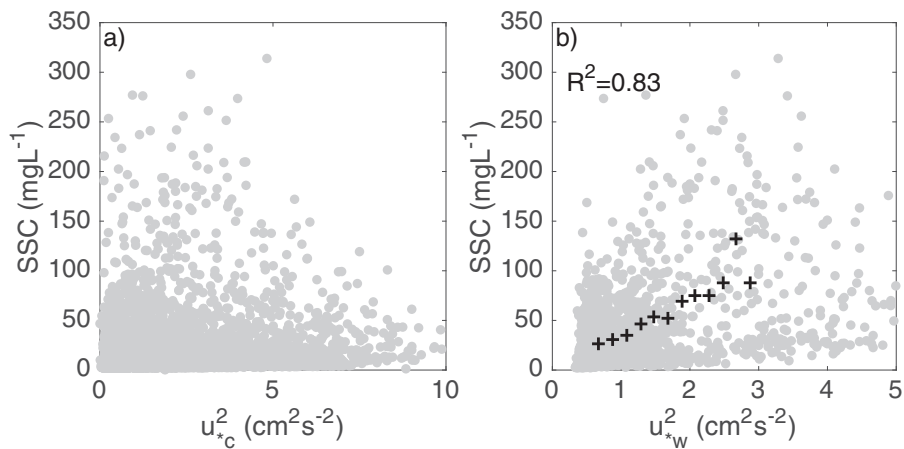


**Figure 5.** SSC versus wave and current friction velocities. (a) SSC versus current friction velocity for the complete data set. (b) SSC versus wave friction velocity  $u_{*w}^2$  when  $u_{br} > 5 \text{ cm s}^{-1}$ . Data every 15 min was binned on  $u_{*w}^2$  (black crosses).  $R^2$  value corresponds to the binned data.

concentrations are observed, SSC is strongly correlated with the wave stresses ( $R^2 = 0.83$ ) suggesting that waves are primarily responsible for resuspension and the elevated near-bottom concentrations observed at the 12 m site (Figure 5b). When wave-current interaction was considered, no significant improvement in correlation was observed (not shown here), however, the magnitude of the total shear stress was at times much greater than stresses due to waves acting alone.

Near-surface suspended sediment concentrations are much lower than near-bottom concentrations and are less variable. When stratification is reduced during storms, peak near-surface concentrations can reach up to  $50 \text{ mgL}^{-1}$  as sediment is mixed from the bottom (Figure 4d). During calm periods near-surface concentrations were on the order of  $10 \text{ mgL}^{-1}$  and remarkably constant, particularly during stratified neap tide conditions. After day 280 an increase in background concentration is observed (Figure 4d), for both near-bottom and near-surface signals, which is attributed to the reduction in stratification and the presence of a very shallow pycnocline (Figure 4a). Nevertheless, near-surface concentrations were still below  $25 \text{ mgL}^{-1}$ .

Near-bottom cross-shore fluxes result in a net export of suspended sediment by the end of the observational period, but the direction and intensity of transport was variable (Figures 6a and 6b). Though density-driven cross-shore velocities during stratified neap tides can be relevant as a consequence of tidal straining, the corresponding transport at depth is very small as a result of low sediment concentrations (Figure 6a, days 260–264 and 273–280).

Significant net offshore transport is observed during both storms (days 264–266 and 280–284), however, the transport direction varied within those periods. High cross-shore sediment fluxes during storms are the result of very high suspended sediment concentrations, since the absence of stratification resulted in a considerable reduction of the cross-shore currents.

Near-bottom transport during spring tides is much higher relative to the transport observed during neap tides. The direction of net (cumulative) transport during spring tide was variable; net onshore transport was observed during days 266–270, and offshore transport was observed during days 284–288. It is of note that the system is effectively reset by stratified spring transport after the big storm of days 264–266, as the onshore fluxes brought back an equivalent amount of sediment to what was previously exported during the storm (Figures 6a and 6b).

The cumulative near-surface cross-shore sediment transport was always directed seaward (Figure 6b). The intensity of near-surface transport was relatively constant, with increased transport during storms, most notably during days 280–284 as a result of increased background concentrations. The overall magnitude of near-surface transport is approximately four times greater than net transport at depth, which is attributed to persistent offshore flows near the surface as a result of the density-driven circulation.

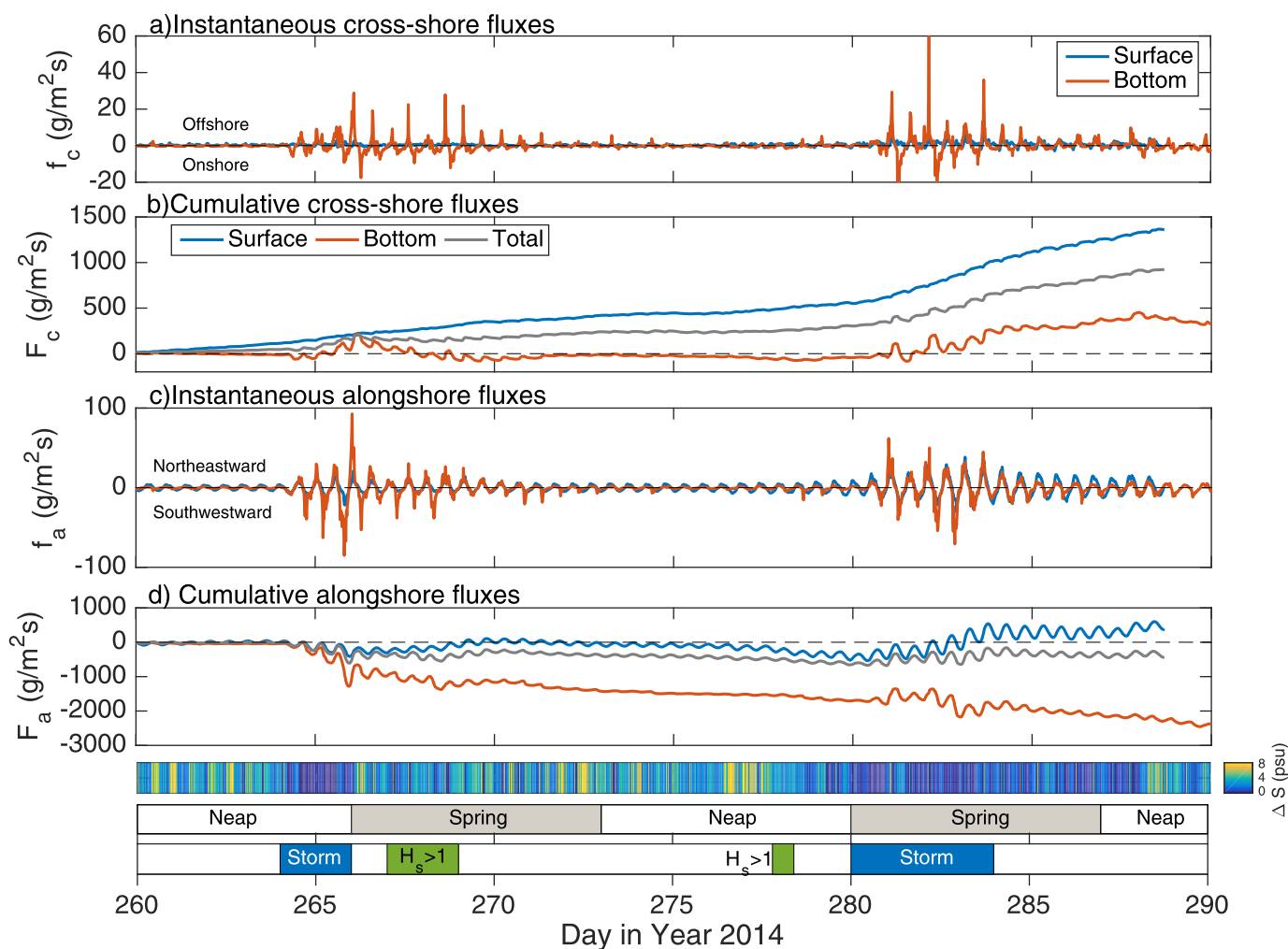


**Figure 6.** Near-bottom, near-surface, and total (top to bottom) suspended sediment fluxes. (a) Instantaneous cross-shore fluxes. (b) Cumulative cross-shore fluxes. (c) Instantaneous alongshore fluxes. (d) Cumulative alongshore fluxes. In all plots, the red line represents near-bottom fluxes and the blue line represents near-surface fluxes. In Figures 6b and 6d the gray line represents the (top to bottom) cumulative total flux. Bottom bars show vertical stratification in terms of top-bottom salinity difference  $\Delta S$  (psu), neap/spring, and storm periods, and the occurrence of  $H_{sig} > 1$  (m).

Net near-bottom alongshore sediment transport was always directed to the southwest (Figure 6d), with episodes of elevated transport during storms (Figure 6c). The magnitude of transport was higher than the corresponding cross-shore transport, as alongshore velocities are much higher and do not depend on the mean state of stratification. By the end of the deployment, the near-surface cumulative alongshore transport was directed toward the northeast (Figure 6d), however, it was much smaller than transport at depth. Tidal asymmetries seem to be responsible for the shift in direction between neap and spring tides; during neap tides, a longer ebb duration dominates over higher flood velocities and results in southward transport, and during spring tides, higher flood velocities dominate over the effect of a longer ebb duration resulting in northward transport.

Total (top to bottom) cross-shore sediment flux was directed offshore, while the total alongshore transport was directed to the southwest (Figures 6b and 6d), similar to what was reported by Horner-Devine et al., [2017] based on field work in winter 2013.

#### 4.3. Near-Bottom Cross-Shore Transport Mechanisms

In this section, we focus in detail on distinct periods in the record to identify the mechanisms that generate cross-shore transport at depth, and specify the forcing conditions under which they occurred. We describe three transport mechanisms; the observed water column response and a conceptual schematic for each are presented in Figures 7–11.

It is worth mentioning that in this section, we describe the clearest transport signals, but that other mechanisms were observed in addition to the ones presented here. In particular, we observed periodic peaks in near-bottom suspended sediment concentrations occurring approximately 30–60 min after flow reversal that are not timed with high flow velocity or high bed stresses. These peaks appear to be the result of an eddy that forms on the flood phase of the tide on the lee side of the Sand Engine [Radermacher *et al.*, 2016] and advects sediment offshore as the tidal velocities reverse. The formation of the eddy is similar to that reported by Geyer and Signell [1990] for tidal currents around a headland. This signal was clearest during calm neap tides (days 260–264), as background concentrations were low, but resulted in negligible transport when compared to the mechanisms described in the following subsections (Figure 6b).

#### 4.3.1. Storm Transport

Our measurements included two significant storms that are typical of the fall season along the Dutch coast and have a large impact on coastal suspended sediment concentrations (Figure 4d). Sediment transport during storm events results from the combination of high near-bottom sediment concentrations, primarily as a result of wave-induced resuspension, and weak cross-shore currents. Sediment availability dominates over the fact that cross-shore currents are very small, yielding high sediment fluxes with transport preferentially directed offshore.

The local response of salinity, velocity, bed stresses, and suspended sediment concentrations during the first storm period (days 264–266) is examined in detail in Figure 7. Stratification is nearly zero during the storm as high winds and waves mix out the water column (Figure 7a). Under well-mixed conditions, tidal currents are primarily rectilinear and coast parallel according to the progressive Kelvin wave character of the semidiurnal tide along the Dutch coast [Simpson, 1997]. However, as shown by De Boer *et al.* [2006], small ellipticities are still present due to Earth's rotation and the proximity of the coastal wall. As a result, very weak cross-shore currents still occur, particularly near the bottom, with maxima below  $0.1 \text{ ms}^{-1}$ . Tidal current asymmetry (with higher flood velocities) and the absence of tidal straining and results in higher offshore velocities occurring during the flood phase of the tide.

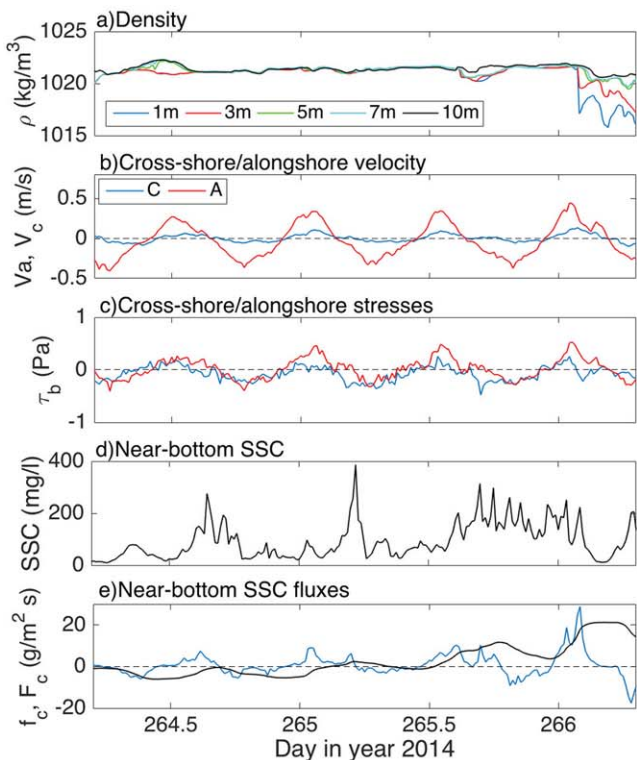


**Figure 7.** Storm transport. (a) Salinity, 12 m mooring. (b) Near-bottom cross-shore (blue line) and alongshore (red line) velocities. (c) Bottom cross-shore (blue line) and alongshore (red line) stresses. (d) Near-bottom suspended sediment concentration. (e) Instantaneous (blue line) and cumulative (black line) near-bottom SSC fluxes. Cumulative sediment flux has been scaled for plotting purposes. (f) Schematic of transport process.

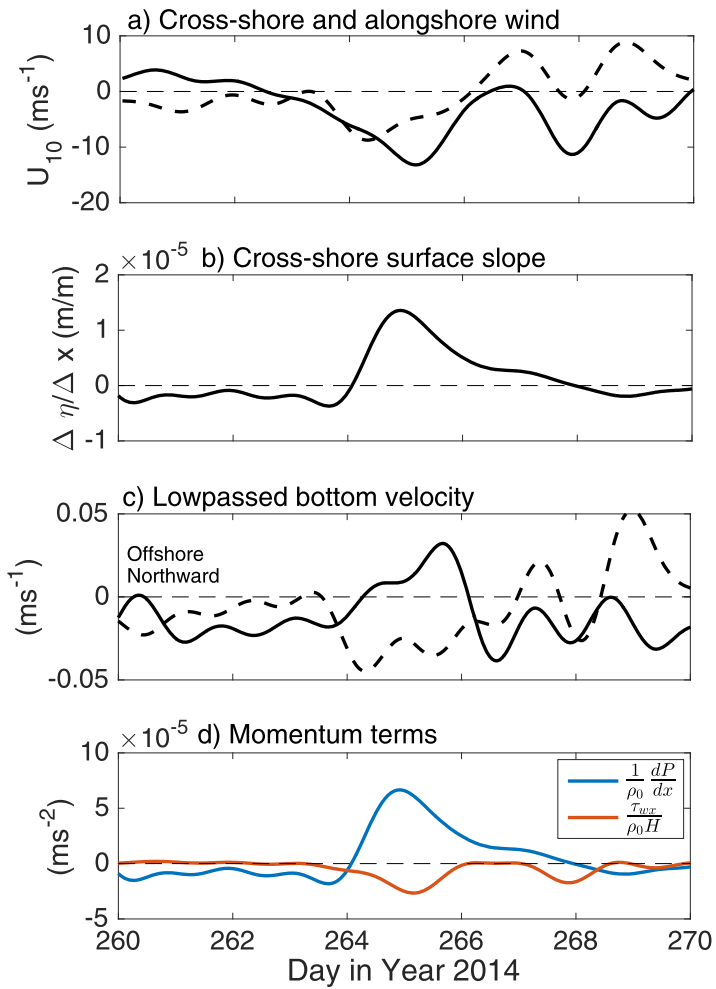


**Figure 8.** Wind forcing during storm 1. (a) Cross-shore wind (solid line) and alongshore wind (dashed line). Positive cross-shore wind is directed offshore and positive alongshore wins is directed northwards. (b) Low-passed cross-shore sea surface slope, computed from ADCP depth measurements at 18 and 12 m. (c) Low-passed near-bottom cross-shore (solid line) and low-passed near-bottom alongshore velocity (dashed line). Positive cross-shore velocity is directed offshore and positive alongshore velocity is directed northward. (d) Wind (red line) and pressure gradient (blue line) terms from the depth-averaged cross-shore momentum balance.

entire water column, except for a thin surface layer ( $\sim 1\text{--}2$  m) flowing onshore. We hypothesize that this current structure is the result of a cross-shore barotropic pressure gradient associated with wind-induced coastal setup. We estimate the cross-shore sea surface slope using the residuals from a harmonic analysis fit performed to the ADCP depth measurements at our 18 and 12 m locations, which are separated by 3.5 km (Figures 8a and 8b). Sea surface slope is strongly correlated with observed variations in near-bottom low-passed cross-shore and alongshore velocities (Figures 8b and 8c). A residual offshore flow is observed during days 264–266, with a 16 h delay between maximum setup and maximum cross-shore residual velocity. Onshore propagating waves can also contribute to the mean offshore flow at depth in response to the onshore Stokes' drift at the surface [Lentz et al., 2008; Fewings et al., 2008].

Gutierrez et al. [2006] suggest that the relative strength of the wind and pressure gradient terms in the momentum equation influences the structure of the flow in the inner shelf; flow opposes the wind when the pressure gradient term exceeds the wind stress term. Comparison of the wind stress and setup terms in the depth-averaged cross-shore momentum balance for our data shows that the pressure gradient is in fact large enough during the first storm to drive flow against the wind through most of the water column (Figure 8d). The difference between these two momentum terms is expected to be due to the contributions

During this unstratified period, the cross-shore velocities are reduced compared to the previous stratified neap tide period, are almost in phase with the alongshore velocities, revealing the absence of tidal straining (Figure 7b). Peaks in suspended sediment concentration are not aligned with the peaks in tidal velocity or stress, suggesting that tidal motions are not sufficient on their own to generate the observed resuspension (Figures 7b–7d). We conclude that resuspension is primarily wave-induced. Offshore (positive) cross-shore velocities are larger than the onshore velocities (Figure 7b), even though onshore (negative) velocities persist longer. Because suspended sediment concentrations remain elevated during this period the asymmetry in the velocity magnitude contributes to the net offshore transport during this 2 day period (Figures 6e and 7e).

In addition to tidal currents, cross-shelf winds contribute to cross-shelf exchange during storms. Strong onshore winds occurred during the first storm (days 264–266), with wave heights on the order of 2 m. During this period, cross-shore currents are offshore through the

from bottom stress and wave radiation stresses, both of which are expected to be high during storms, and Earth's rotation.

Offshore winds during the second storm (days 280–284) also generate a persistent offshore flow through most of the water column. The situation is different from the previous storm, however, in that the flow follows the wind direction. Low-passed near-bottom cross-shore velocities are directed offshore (not shown) and their magnitude is on average larger than those observed during the first storm, probably due to the alignment of the wind and wave forcing [Fewings *et al.*, 2008]. It is also important to note that the second storm occurs during spring tide so offshore directed tidal currents are larger. No data are available to compute the pressure gradient during the second storm since the ADCP at our 18 m mooring stopped working around day 279.

#### 4.3.2. Frontal Transport

The passage of distinct freshwater lenses at the surface, and the fronts that bound them, is an important dynamical component of the midfield region. Implications for sediment transport have been previously reported by Horner-Devine *et al.*, [2017] and were described in section 2. Figure 9 illustrates the frontal pumping mechanism for a single tidal cycle, where the observed lag ( $\sim 0.5$  h) between the drop in salinity at the plume front and peak suspended sediment concentrations (Figures 9a and 9d) is interpreted as the plume pumping wave-suspended sediment from the inshore. Bed stresses (Figure 9c) are low when the plume passes over our instruments, confirming that the suspended sediment peak is not due to local resuspension and is instead the result of advection from inshore. Our observations show that cross-shore transport driven by frontal dynamics is significant only during spring tides with low to moderate wind forcing (wind speeds lower than  $\sim 10 \text{ ms}^{-1}$ ), such that the freshwater lens is not driven offshore or rapidly mixed with ambient ocean waters.

In addition to the frontal pumping mechanism, our turbulence measurements show that near-bottom turbulence spikes during frontal passages. In particular, the cross-shore component of the Reynolds stresses

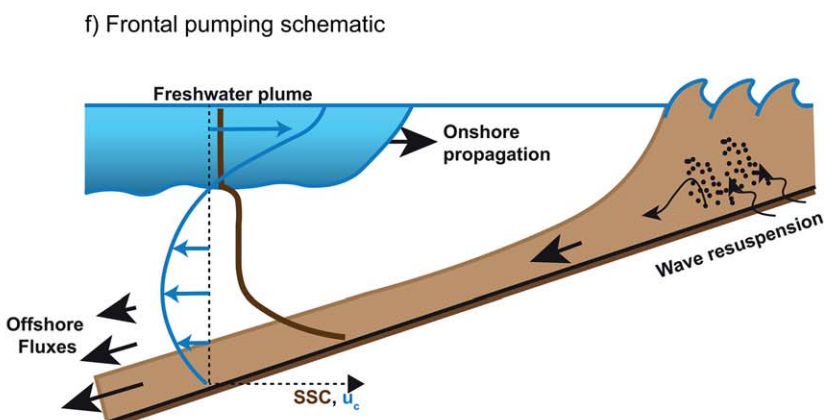
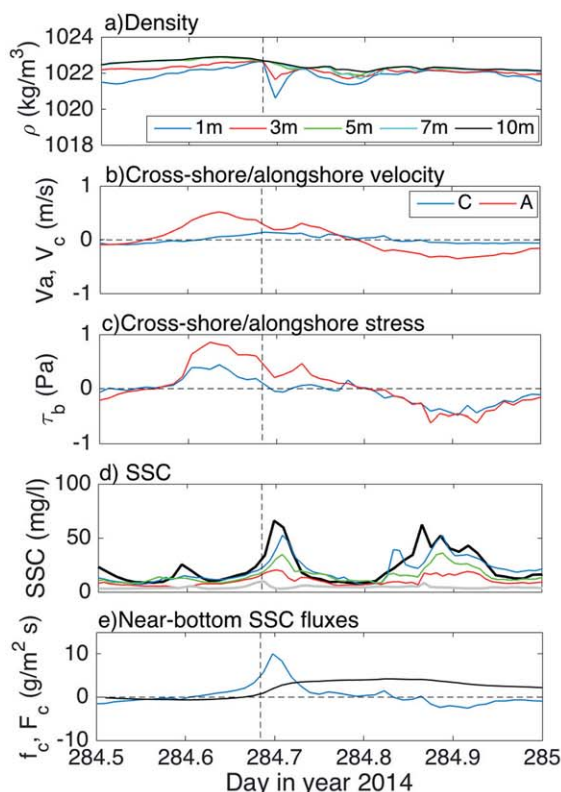


**Figure 9.** Frontal pumping. (a) Density. (b) Cross-shore (blue line) and alongshore (red line) near-bottom velocities. (c) Cross-shore (blue line) and alongshore (red line) bottom stress. (d) Suspended sediment concentration. Black line represents near-bottom concentration, blue line represents 3 m above bottom, green line is 5 m ab, red lines is 7 m ab, and gray line is surface concentration. (e) Instantaneous (blue line) and cumulative (black line) near-bottom cross-shore fluxes. Vertical-dashed line represents the arrival time of the front. (f) Schematic of transport mechanism.

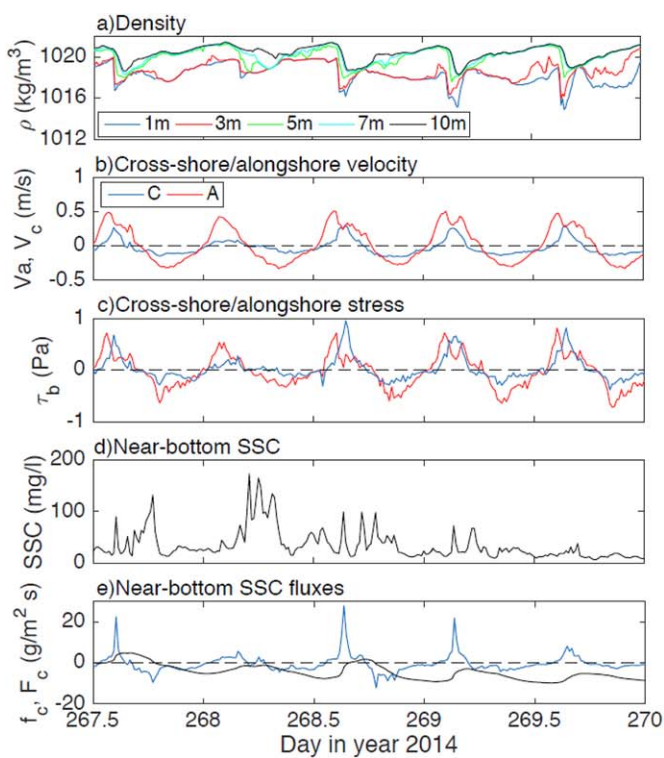
( $u'w'$ ) exhibits peaks right when the freshwater plume passes over the instruments. This effect can be seen in Figure 10c, which is intended to describe transport processes during a stratified spring tide period (see section 4.3.3) but shows significant frontal activity. Peaks in  $u'w'$  are often timed with peaks in near-bottom sediment concentration suggesting local resuspension of sediment and subsequent offshore advection due to the passing of the tidal plume front (Figures 10c and 10d). It is worth noting that the increase in bottom turbulence is only observed during the passage of thick fronts with cross-shore propagation speed on the order of  $0.4\text{--}0.5\text{ ms}^{-1}$ . This process likely becomes even more important as the front propagates to shallower depths, as stresses could be further increased resulting in enhanced resuspension.

The net effect of frontal processes therefore is to generate offshore sediment transport (Figure 9d), by means of high offshore flux pulses that can be readily identified in the near-bottom sediment fluxes (Figure 6a, days 266–270).

#### 4.3.3. Stratified Tidal Transport

Stratification is expected to strongly influence transport processes in ROFs. Here we define stratified tidal transport as those transport processes occurring during stratified periods at timescales longer than the passage of the tidal plume front. During stratified periods, observed near-bottom cross-shore currents are predominantly directed onshore resulting in net onshore sediment transport.

High cross-shore transport at depth is observed during spring tide days 267–270 with moderate downwelling wind forcing. A distinct two-layer density structure is observed with cross-shore flow driven by large horizontal density gradients resulting in the onshore movement of denser water close to the bottom (see section 4.1). Surface and bottom mixing due to winds, waves, and spring tides contribute to mixing the upper and lower layers, resulting in a 3–4 m thick surface layer and a 7–8 m thick bottom layer of uniform density that breaks down only when the plume front passes through our field site (Figure 10a). The effect of the tidal plume front can be clearly observed in the near-bottom cross-shore velocity and sediment fluxes (Figures 10b and 10d) as described in section 4.2. No apparent tidal variability is observed in the suspended sediment concentrations (Figure 10d), suggesting that waves and advection are responsible for concentrations exceeding  $100\text{ mg L}^{-1}$ . The density-driven circulation profile results in onshore velocities and sediment



f) Stratified Spring Transport

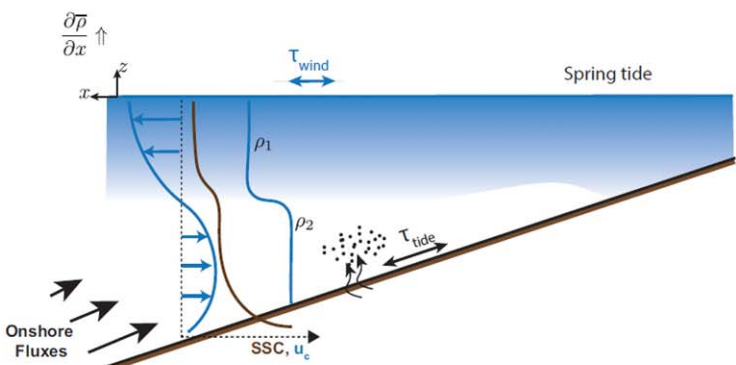


**Figure 10.** Stratified spring transport. (a) Salinity, 12 m mooring. (b) Cross-shore and alongshore velocity. (c) Cross-shore and alongshore bottom stresses. (d) Near-bottom SSC. (e) Near-bottom suspended sediment fluxes, instantaneous (blue) and cumulative (black, scaled). (f) Schematic of transport process during stratified spring tide after frontal passage.

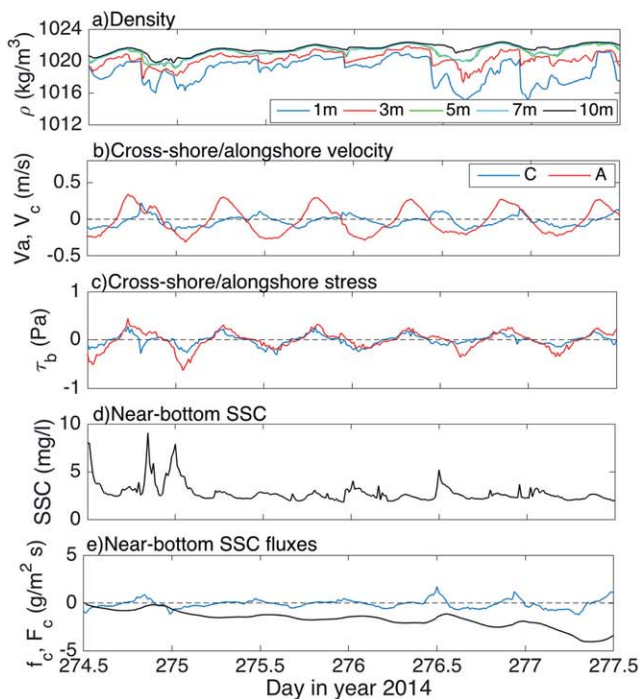
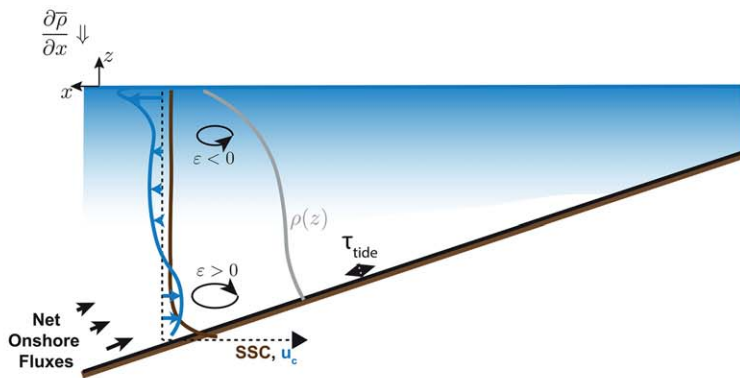


**Figure 11.** Stratified neap transport. (a) Density at 12 m mooring. (b) Near-bottom cross-shore velocity. (c) Near-bottom suspended sediment concentration. (d) Near-bottom cross-shore suspended sediment fluxes. Blue line represents the instantaneous flux and black line represents the cumulative sediment flux. (e) Schematic of transport mechanism.  $\varepsilon$  represents ellipticity (see section 5.3 for definition).

f) Stratified neap transport schematic



transport in the lower layer that persist for most of the tidal cycle (Figures 10b and 10e). Despite the fact that the magnitude of onshore transport is typically much less than the transport peaks resulting from frontal dynamics, the cumulative transport is dominated by persistent onshore fluxes resulting from the density-driven flow (Figure 10e).

Cross-shore tidal straining dynamics appear to gain importance during the more vertically stratified neap tides, as has been previously reported for the far-field [De Boer et al., 2006; Simpson and Souza, 1995] when cross-shore horizontal density gradients are not particularly high. For these periods, the tidal ellipses are more circular than during storm or spring tide periods (anticyclonic near the surface and cyclonic near the bottom) with current patterns that are not symmetrical as in the far-field region, and we observe that the timing of offshore/onshore directed currents also differs. Figure 11 examines in detail the local response under stratified neap tide conditions. Cross-shore and alongshore currents are out of phase due to effect of vertical stratification and cross-shore current asymmetry, favoring onshore velocities near the bottom (Figure 11b), results in net onshore sediment fluxes (Figure 11d). However, the magnitude of transport is negligible when compared to transport during spring tide due to low sediment concentrations (Figure 11d) resulting from low wave forcing and low tidal stresses.

## 5. Discussion

### 5.1. Net Transport and the Role of Individual Transport Mechanisms

In this section, we examine the net cross-shore transport, considering in particular the relative contributions of each of the transport mechanisms described in section 4. The direction of cross-shore transport switches and its magnitude changes several times during the observational period (Figure 12b) as the dominant transport mechanisms turn on and off in response to the tidal, wind and wave forcing. Storm transport is dominant when wind and wave conditions are sufficient to homogenize the water column and preferentially transports near-bottom sediment offshore during our study period. Frontal transport is active under moderate to low wind conditions and during spring tides, and preferentially transports near-bottom sediment offshore. Stratified spring and neap tide transport preferentially transports near-bottom sediment onshore, although the magnitude of cross-shore transport during neap tides is very low.

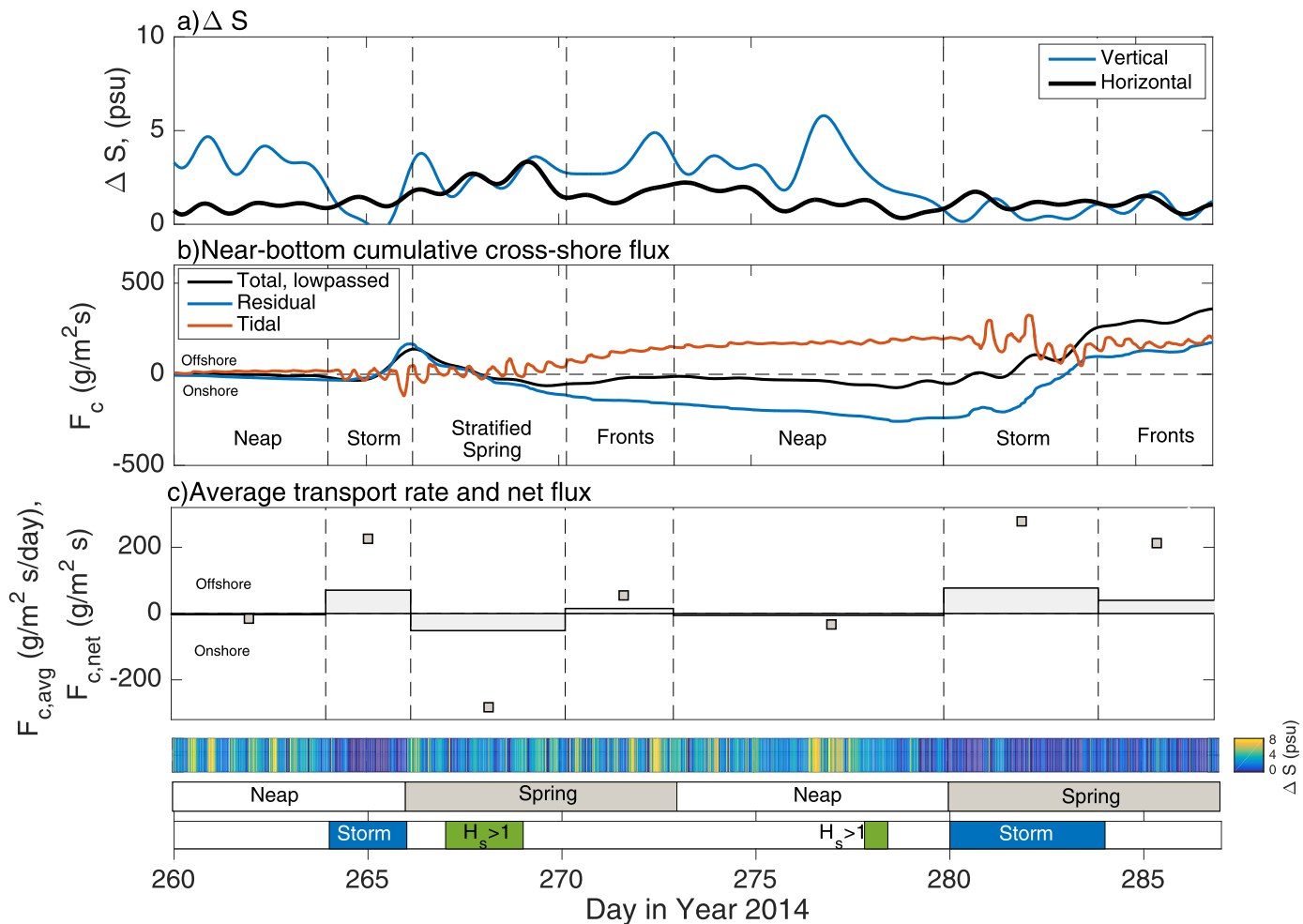


**Figure 12.** Drivers of cumulative cross-shore flux. (a) Top-bottom salinity difference (blue line) and mean horizontal salinity difference between 18 m mooring and 12 m mooring (black). (b) Near-bottom cumulative cross-shore flux (black line), near-bottom cumulative tidal flux (red line), and near-bottom cumulative residual flux (blue line). (c) Average transport rate (bars) and net transport (squares) in each period. Bottom bars show vertical stratification in terms of top-bottom salinity difference  $\Delta S$  (psu), neap/spring, and storm periods, and the occurrence of  $H_{\text{sig}} > 1$  (m).

Net transport results from the combination of these different modes, which contribute to onshore or offshore fluxes at different rates. Net transport by the end of our deployment was offshore, however, significant episodes of landward transport were observed (Figure 12b) as the forcing conditions changed in time. Figure 12c provides a basis for comparing the relative strength of each process in terms of the observed transport rates and the total transport during each period. The highest transport rates are observed during storms, with the first storm being particularly intense and contributing almost as much net transport as the second storm in approximately half of the time. Net transport and transport rates during both spring tide periods were also significant. The stratified spring period following the first storm transports more sediment landward than is transported seaward by the preceding storm. Transport is also significant during the second spring tide; however, it is directed offshore due to reduced stratification at our site as the whole plume was displaced toward the north and the influence of the fronts. In all, the net transport during the two storm periods accounts for 45% of the total transport over the observational period; transport during the stratified spring tide and transport during the frontal periods account for 25% and 15% of the total, respectively.

It is important to note that the observed transport mechanisms often occur at the same time, reinforcing or competing with each other, or may influence subsequent periods by modifying ambient conditions. For example, both spring tide periods in our study are influenced by preceding storm conditions, which may

impact transport processes after their occurrence. The episode of elevated landward transport due to stratified spring tide transport occurring after the first storm is likely influenced by the storm itself, as sediment may remain in suspension or be easily resuspended during the days that follow. Also, plume fronts often propagate on a vertically and horizontally stratified ROFI, and the magnitude and direction of transport results from the interaction of these processes. A clear example of this is observed during the stratified spring transport period that follows the first storm (days 266–270; Figure 10). During this period, strong plume fronts compete with cross-shore currents resulting from large horizontal density gradients, such that the seaward transport resulting from frontal processes is countered by onshore tidal transport. Although frontal processes generate very large pulses of seaward transport, landward transport is more persistent and ultimately results in a net landward transport during this period. Interestingly, the direction of transport switches to offshore toward the end of this spring tide period. Detailed examination of the data suggests that the transport during this latter period is more pulsed, suggesting that fronts may play an increasingly important role.

As noted in section 4.3, additional transport due to the formation and advection of a headland eddy as a consequence of the interaction of the tidal currents and the Sand Engine is evident on our measurements, but yielded no significant contribution to the overall cumulative near-bottom transport (see days 260–264 in Figure 12b).

### 5.2. Relevance of Frontal Pumping

Frontal pumping was found to be the dominant mechanism of cross-shore transport of fines at depth in a field experiment conducted in the same location in winter 2013 during a period when wind and wave forcing was moderate *Horner-Devine et al.*, [2017]. One objective of this study is to investigate whether plume pumping is the dominant transport mechanism under a different set of forcing conditions.

We observe that most of the cross-shore transport at depth occurs during days 264–270 and days 280–287 (Figures 6a and 6b). The first period is strongly influenced by the energetic storm of days 264–266; however, the signature of frontal processes is clear during days 267–270 (spring tide) where significant pulses in offshore transport are observed. As described in section 5.1, cumulative transport during days 267–270 is directed onshore, despite the seaward transport pulses. During days 280–287 (spring tide) net near-bottom transport is offshore, and again it is strongly influenced by the storm-induced sediment concentrations of days 280–284. However, the situation is different from the previous spring tide in that net transport after day 284 continues to be in the offshore direction. After the storm, the rate of transport decreases but it is still dominated by offshore pulses (Figure 6a)), and a detailed inspection of this period (Figure 9) reveals the continuous occurrence of frontal pumping, though not as strong as observed during days 267–270.

From our observations, we conclude the following: frontal pumping is significant during spring tides and contributes to seaward sediment transport. It produces cross-shore fluxes comparable in magnitude to those observed during storms. However, when considering a frontal period, such as days 267–270, frontal transport will sometimes compete with other transport mechanisms and will not necessarily dominate the transport signal. In particular, we observe that frontal pumping dominates when the ambient stratification is low, as observed in 2013 [*Horner-Devine et al.*, 2017] and in the second spring period (days 284–287), but that its impact is diminished in the presence of higher persistent stratification.

### 5.3. Role of Stratification

The role of stratification on the direction of net transport can be better understood in terms of a mean state of vertical stratification, at timescales equal or longer than the tidal period. Figure 12a shows the time series of top-bottom salinity difference (1 and 10 m below the surface) at the 12 m site and depth-averaged horizontal salinity difference between the 18 and 12 m sites. The data were low-pass filtered to remove variability at tidal and shorter time scales, thus removing the influence of the plume fronts. The relation between cross-shore transport and the mean state of stratification can be observed in Figures 12a and 12b; stratification leads to onshore transport at depth whereas mixed periods lead to seaward transport. It is important to note the role of high winds in destroying stratification and also influencing current structure. The water column tends to be strongly stratified for over half of the deployment ( $\Delta S \sim 4\text{--}5 \text{ psu}$ ); however, negligible sediment concentrations during neap tides result in only one stratified period with significant transport.

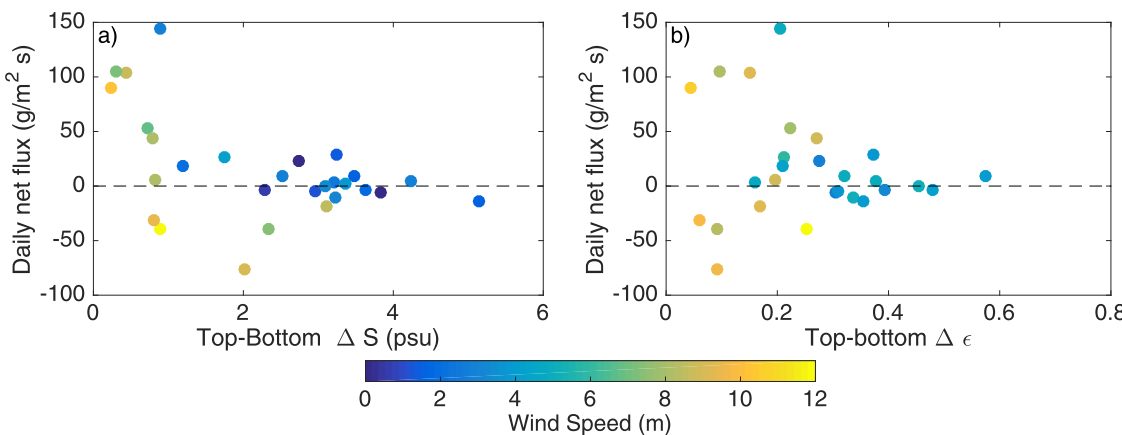


**Figure 13.** Stratification and bottom sediment fluxes. (a) Top-bottom salinity difference (averaged over a day) versus daily net flux. (b) Top-bottom ellipticity difference versus daily net flux. Colors indicate mean wind speed (averaged over a day).

One effect of stratification and the straining of the density field is the generation of residual currents [Stacey *et al.*, 2001; Burchard and Hetland, 2010], which also contributes to the trends observed in Figure 12. The decomposition of the observed velocities into tidal and residual components (Figure 12b) reveals that bottom sediment fluxes are in large part dominated by the residual transport. In this region, tidal straining processes are asymmetric and tend to favor onshore currents near the bottom. The density-driven circulation also induces onshore currents in the near-bottom layer. When these processes occur, that is, when stratification is present, residual velocities and associated transport are directed landward. On the other hand, when stratification is significantly reduced (or completely eliminated), the velocity field characteristic of tidal straining circulation breaks down, cross-shore shear decreases and the velocity is vertically unidirectional. Under conditions of strong meteorological forcing, the tidal asymmetry with higher flood velocities and an offshore mean flow created by coastal setup and waves led to seaward net transport over the tidal cycle.

Tidal straining is the dominant process influencing the dynamics of bottom-attached plume systems such as the Rhine ROFI, and it is clear that the tidal straining velocities far from the river mouth influence the movement of sediment [Joordens *et al.*, 2001; van der Hout *et al.*, 2015]. In the following, we consider the importance of tidal straining on sediment transport in this midfield plume region. Ellipticity, defined as the ratio of minor to major axis of the tidal ellipses (negative for anticyclonic rotation), has been considered as a metric of tidal straining [De Boer *et al.*, 2008] as it quantifies the deviation from the rectilinear current pattern typical of a progressive Kelvin wave ROFI regime (with zero ellipticity) as a result of vertical stratification. Periods of strong vertical stratification show high counterrotating ellipticity in the upper and lower layers and very high top-bottom ellipticity difference, whereas the opposite is true for well-mixed periods. Figure 13 shows the relation between the mean state of stratification and net sediment fluxes in terms top-bottom ellipticity difference and top-bottom salinity difference. Wind speed has been included as an indicator of meteorological stirring and the occurrence of storms. Calculation of ellipticity requires the use of a moving window tidal harmonic analysis, and each data point corresponds to a 25 h period. The highest sediment fluxes are observed at very low ellipticity and salinity differences values ( $\Delta \epsilon < 0.1$  and  $\Delta S < 1 \text{ psu}$ ) and high wind speeds, suggesting that barotropic processes dominate near-bottom cross-shore transport during this period. Intermediate ellipticities and salinity differences (see  $1 < \Delta S < 3$ ) during spring tides with moderate to low wind forcing also result in significant cross-shore transport, suggesting that baroclinic processes are also important to cross-shore transport. However, sediment fluxes are severely reduced for values of  $\Delta \epsilon > 0.3$ , corresponding primarily to stratified neap tide periods under weak wind forcing, and  $\Delta S > 3 \text{ (psu)}$ . This suggests that tidal straining on its own does not contribute significantly to the net cross-shore sediment flux in the midfield plume region during this period. The reason for this is that strong vertical stratification and tidal straining occur during low energy periods, when sediment concentrations are low. Indeed, analysis of the neap tide data (not shown) confirm that there is a residual onshore velocity that is sufficient to generate onshore sediment flux of a similar magnitude to the spring tide and storm fluxes, if the near-bed sediment concentration were similar to that observed under more energetic conditions.

It is interesting to note that near-bottom cross-shore transport was very low during unstratified conditions in 2013 and significant transport was only observed during periods of strong frontal activity, which accounted for more than 85% of the total transport during that measurement period [Horner-Devine *et al.*, 2017]. Sampling in winter 2013 followed a period of very stormy conditions and we hypothesize that the difference in behavior is a result of lower sediment availability on the bed in 2013 because of these preceding storms. This hypothesis is supported by the observations that average near-bottom sediment concentrations in the winter 2013 sampling period were less than half those observed in fall 2014. It is likely that sediment accumulates on the seabed during the calmer summer months, resulting in higher concentration of suspended sediment during the first storms in the fall.

## 6. Conclusions

We used detailed measurements of density, suspended sediment concentration, and current structure to investigate transport processes in the midfield region of the Rhine River plume. This work establishes how tidal, wind, and wave forcing in a region strongly influenced by river-generated density stratification result in along and across-shore sediment transport. Furthermore, we identify the dominant mechanisms driving the cross-shore transport of fine sediments at depth. The work has particular significance because the measurements were made in the vicinity of the Sand Engine, a mega-nourishment project that could potentially change coastal protection practices. The primary conclusions of the work are as follows:

1. During the 4 week study period in fall 2014, cumulative suspended sediment fluxes near the surface were offshore and upcoast (northeast). Cumulative fluxes near the bed were offshore and down coast (southwest). Cumulative top to bottom fluxes were offshore and down coast.
2. Three mechanisms of cross-shore transport at depth were observed. Net transport results from the combination of these mechanisms as they turn on and off in response to the forcing conditions, and the relative importance of each mechanism explains the variability observed in both magnitude and direction of transport.
3. Storms contribute most to the cross-shore sediment transport during the observation period. During those periods, the water column is vertically well-mixed and high waves play a dominant role in sediment resuspension. Barotropic transport during storms accounts for almost half of the observed transport at depth and results in net offshore transport. The occurrence of cross-shelf winds generated a coastal setup that contributed substantially to the offshore flux of fine sediment.
4. During stratified periods, transport at depth depends on wind magnitude and direction, which set the location of the freshwater plume, determine the strength of the cross-shore density gradients and the strength of the fronts. Tidal straining on its own does not appear to generate significant sediment transport as it is strongest during neap tides when vertical stratification is higher and sediment concentrations are very low. Net transport during stratified periods is onshore.
5. Tidal plume fronts are clearly observed in density and cross-shore velocity profiles, presenting a dynamical component not observed in the far-field. Their contribution to sediment transport is only significant during spring tides, when they manifest as strong pulses of seaward transport at depth that can be of similar magnitude to storm fluxes. However, the overall effect of fronts on net transport depends on the mean state of stratification; net seaward transport due to fronts is only realized when the ambient coastal stratification, which generates onshore transport, is low.
6. Over the course of the measurement period, near-bottom suspended sediment flux is offshore during unstratified periods, primarily due to storms and to a lesser degree fronts, and onshore during persistently stratified periods, primarily during spring tide. Net cross-shore transport was offshore during our observation period; however, the magnitude of the onshore and offshore transport mechanisms was close enough that a different combination or sequence of forcing conditions could conceivably result in net shoreward transport instead.

Overall, we conclude that both barotropic and baroclinic dynamics are relevant for sediment transport processes in the midfield region of the Rhine ROFI. On longer time scales, we expect seaward transport to dominate during winter time as the water column would tend to be mixed more frequently. On the contrary, calm weather during summer time would lead to shoreward transport because increased stratification could be expected.

### Acknowledgments

The authors would like to thank Maggie McKeon, Saulo Meirelles, Martijn Henriquez, Richard Cooke, Christopher Balfour, and the crew of the R/V Zirfaea for their technical support during the measurements, Ad Stolk and Rijkswaterstaat for their generous and kind support, and Onno van Tongeren and Wil Borst from the Port of Rotterdam. The authors are grateful for support from the Netherlands Organization for Scientific Research STW program Project 12682 Sustainable engineering of coastal systems in Regions of Freshwater Influence and ERC-advanced grant 291206 Nearshore Monitoring and Modeling (NEMO). R.P.F. would like to thank the Fulbright Commission and CONICYT-Chile for the scholarship provided. A.R.H.-D. was supported by the Allan and Inger Osberg Professorship. A.J.S. was funded by NERC through NOC National Capability funding. The authors are also grateful for support provided by NERC to deploy the Mini STABLE frame. Last, the authors appreciate the valuable input received from two anonymous reviewers, which helped to substantially improve this manuscript. Data from this paper are available upon request. Please contact Raúl P. Flores at rfloresa@uw.edu.

### References

- Burchard, H., and R. D. Hetland (2010), Quantifying the contributions of tidal straining and gravitational circulation to residual circulation in periodically stratified tidal estuaries, *J. Phys. Oceanogr.*, 40(6), 1243–1262.
- Dagg, M., R. Benner, S. Lohrenz, and D. Lawrence (2004), Transformation of dissolved and particulate materials on continental shelves influenced by large rivers: Plume processes, *Cont. Shelf Res.*, 24(7), 833–858.
- De Boer, G. J., J. D. Pietrzak, and J. C. Winterwerp (2006), On the vertical structure of the rhine region of freshwater influence, *Ocean Dyn.*, 56(3–4), 198–216.
- De Boer, G. J., J. D. Pietrzak, and J. C. Winterwerp (2008), Using the potential energy anomaly equation to investigate tidal straining and advection of stratification in a region of freshwater influence, *Ocean Model.*, 22(1), 1–11.
- De Kok, J. (1996), A two-layer model of the rhine plume, *J. Mar. Syst.*, 8(3), 269–284.
- de Nijs, M. A., J. C. Winterwerp, and J. D. Pietrzak (2010), The effects of the internal flow structure on SPM entrapment in the Rotterdam waterway, *J. Phys. Oceanogr.*, 40(11), 2357–2380.
- de Ruijter, W. P., A. W. Visser, and W. Bos (1997), The rhine outflow: A prototypical pulsed discharge plume in a high energy shallow sea, *J. Mar. Syst.*, 12(1), 263–276.
- de Schipper, M. A., S. de Vries, G. Ruessink, R. C. de Zeeuw, J. Rutten, C. van Gelder-Maas, and M. J. Stive (2016), Initial spreading of a mega feeder nourishment: Observations of the sand engine pilot project, *Coastal Eng.*, 111, 23–38.
- Fewings, M., S. J. Lentz, and J. Fredericks (2008), Observations of cross-shelf flow driven by cross-shelf winds on the inner continental shelf, *J. Phys. Oceanogr.*, 38(11), 2358–2378.
- Fewings, M. R., and S. J. Lentz (2010), Momentum balances on the inner continental shelf at Martha's vineyard coastal observatory, *J. Geophys. Res.*, 115, C12023, doi:10.1029/2009JC005578.
- Fong, D. A., and W. R. Geyer (2001), Response of a river plume during an upwelling favorable wind event, *J. Geophys. Res.*, 106(C1), 1067–1084.
- Fong, D. A., and W. R. Geyer (2002), The alongshore transport of freshwater in a surface-trapped river plume, *J. Phys. Oceanogr.*, 32(3), 957–972.
- Garvine, R. W. (1974), Physical features of the Connecticut river outflow during high discharge, *J. Geophys. Res.*, 79(6), 831–846.
- Garvine, R. W. (1977), Observations of the motion field of the Connecticut river plume, *J. Geophys. Res.*, 82(3), 441–454.
- Garvine, R. W. (1984), Radial spreading of buoyant, surface plumes in coastal waters, *J. Geophys. Res.*, 89(C2), 1989–1996.
- Geyer, W. R. (1993), The importance of suppression of turbulence by stratification on the estuarine turbidity maximum, *Estuaries*, 16(1), 113–125.
- Geyer, W. R., and R. Signell (1990), Measurements of tidal flow around a headland with a shipboard acoustic Doppler current profiler, *J. Geophys. Res. Oceans*, 95(C3), 3189–3197.
- Geyer, W. R., P. Hill, and G. Kineke (2004), The transport, transformation and dispersal of sediment by buoyant coastal flows, *Cont. Shelf Res.*, 24(7), 927–949.
- Goring, D. G., and V. I. Nikora (2002), Despiking acoustic Doppler velocimeter data, *J. Hydraul. Eng.*, 128(1), 117–126.
- Gutierrez, B. T., G. Voulgaris, and P. A. Work (2006), Cross-shore variation of wind-driven flows on the inner shelf in long bay, South Carolina, United States, *J. Geophys. Res.*, 111, C03015, doi:10.1029/2005JC003121.
- Hetland, R. D. (2005), Relating river plume structure to vertical mixing, *J. Phys. Oceanogr.*, 35(9), 1667–1688.
- Horner-Devine, A. R., D. A. Jay, P. M. Orton, and E. Y. Spahn (2009), A conceptual model of the strongly tidal Columbia river plume, *J. Mar. Syst.*, 78(3), 460–475.
- Horner-Devine, A. R., R. D. Hetland, and D. G. MacDonald (2015), Mixing and transport in coastal river plumes, *Annu. Rev. Fluid Mech.*, 47, 569–594.
- Horner-Devine, A., et al. (2017), Cross-shore transport of surf-zone sediment by river plume frontal pumping, *Geophys. Res. Lett.*, doi:10.1002/2017GL073378, in press.
- Joordens, J., A. Souza, and A. Visser (2001), The influence of tidal straining and wind on suspended matter and phytoplankton distribution in the rhine outflow region, *Cont. Shelf Res.*, 21(3), 301–325.
- Kim, S.-C., C. Friedrichs, J.-Y. Maa, and L. Wright (2000), Estimating bottom stress in tidal boundary layer from acoustic Doppler velocimeter data, *J. Hydraul. Eng.*, 126(6), 399–406.
- Lentz, S. J. (1995), Sensitivity of the inner-shelf circulation to the form of the eddy viscosity profile, *J. Phys. Oceanogr.*, 25(1), 19–28.
- Lentz, S. J., and M. R. Fewings (2012), The wind-and wave-driven inner-shelf circulation, *Annu. Rev. Mar. Sci.*, 4, 317–343.
- Lentz, S. J., M. Fewings, P. Howd, J. Fredericks, and K. Hathaway (2008), Observations and a model of undertow over the inner continental shelf, *J. Phys. Oceanogr.*, 38(11), 2341–2357.
- Madsen, O. S. (1994), Spectral wave-current bottom boundary layer flows, *Coastal Eng.*, 94, 384–397.
- McCandless, R., S. Jones, M. Hearn, R. Latter, and C. Jago (2002), Dynamics of suspended particles in coastal waters (southern north sea) during a spring bloom, *J. Sea Res.*, 47(3), 285–302.
- Milliman, J. D., and J. P. Syvitski (1992), Geomorphic/tectonic control of sediment discharge to the ocean: The importance of small mountainous rivers, *J. Geol.*, 100(5), 525–544.
- Pawlowski, R., B. Beardsley, and S. Lentz (2002), Classical tidal harmonic analysis including error estimates in Matlab using t\_tide, *Comput. Geosci.*, 28(8), 929–937.
- Peperzak, L., F. Colijn, R. Koeman, W. Gieskes, and J. Joordens (2003), Phytoplankton sinking rates in the Rhine region of freshwater influence, *J. Plankton Res.*, 25(4), 365–383.
- Pietrzak, J., J. B. Jakobson, H. Burchard, H. J. Vested, and O. Petersen (2002), A three-dimensional hydrostatic model for coastal and ocean modelling using a generalised topography following co-ordinate system, *Ocean Model.*, 4(2), 173–205.
- Pietrzak, J. D., G. J. de Boer, and M. A. Elefeld (2011), Mechanisms controlling the intra-annual mesoscale variability of SST and SPM in the southern north sea, *Cont. Shelf Res.*, 31(6), 594–610.
- Prandle, D. (1982), The vertical structure of tidal currents and other oscillatory flows, *Cont. Shelf Res.*, 1(2), 191–207.
- Radermacher, M., M. A. de Schipper, C. Swinkels, J. H. MacMahan, and A. J. Reniers (2016), Tidal flow separation at protruding beach nourishments, *J. Geophys. Res. Oceans*, 122, 63–79, doi:10.1002/2016JC011942.
- Rijnsburger, S., C. M. Hout, O. Tongeren, G. J. Boer, B. C. Prooijen, W. G. Borst, and J. D. Pietrzak (2016), Simultaneous measurements of tidal straining and advection at two parallel transects far downstream in the Rhine Rofi, *Ocean Dyn.*, 66(5), 719–736.
- Shaw, W. J., and J. H. Trowbridge (2001), The direct estimation of near-bottom turbulent fluxes in the presence of energetic wave motions, *J. Atmos. Oceanic Technol.*, 18(9), 1540–1557.

- Simpson, J. (1997), Physical processes in the Rofi regime, *J. Mar. Syst.*, 12(1), 3–15.
- Simpson, J., and A. Souza (1995), Semidiurnal switching of stratification in the region of freshwater influence of the Rhine, *J. Geophys. Res.*, 100(C4), 7037–7044.
- Simpson, J. H., J. Brown, J. Matthews, and G. Allen (1990), Tidal straining, density currents, and stirring in the control of estuarine stratification, *Estuaries*, 13(2), 125–132.
- Simpson, J. H., W. G. Bos, F. Schirmer, A. J. Souza, T. P. Rippeth, S. E. Jones, and D. Hydes (1993), Periodic stratification in the Rhine Rofi in the north sea, *Oceanol. Acta*, 16(1), 23–32.
- Souza, A. J., and J. H. Simpson (1997), Controls on stratification in the Rhine Rofi system, *J. Mar. Syst.*, 12(1), 311–323.
- Souza, A. J., J. H. Simpson, and F. Schirmer (1997), Current structure in the Rhine region of freshwater influence, *J. Mar. Res.*, 55(2), 277–292.
- Stacey, M. T., J. R. Burau, and S. G. Monismith (2001), Creation of residual flows in a partially stratified estuary, *J. Geophys. Res.*, 106(C8), 17,013–17,037.
- Stive, M. J., et al. (2013), A new alternative to saving our beaches from sea-level rise: The sand engine, *J. Coastal Res.*, 29(5), 1001–1008.
- Swart, D. H. (1974), Offshore sediment transport and equilibrium beach profiles, PhD thesis, TU Delft, Delft Univ. of Technol., Delft, Netherlands.
- Van Alphen, J. (1990), A mud balance for Belgian-Dutch coastal waters between 1969 and 1986, *Neth. J. Sea Res.*, 25(1-2), 19–30.
- Van Alphen, J., W. De Ruijter, and J. Borst (1988), Outflow and three-dimensional spreading of Rhine river water in the Netherlands coastal zone, in *Physical Processes in Estuaries*, pp. 70–92, Springer, Berlin Heidelberg.
- van der Hout, C. M., T. Gerken, J. J. Nauw, and H. Ridderinkhof (2015), Observations of a narrow zone of high suspended particulate matter (SPM) concentrations along the Dutch coast, *Cont. Shelf Res.*, 95, 27–38.
- Verspecht, F., T. P. Rippeth, J. H. Simpson, A. J. Souza, H. Burchard, and M. J. Howarth (2009), Residual circulation and stratification in the Liverpool bay region of freshwater influence, *Ocean Dyn.*, 59(5), 765–779.
- Verspecht, F., J. Simpson, and T. Rippeth (2010), Semi-diurnal tidal ellipse variability in a region of freshwater influence, *Geophys. Res. Lett.*, 37, L18602, doi:10.1029/2010GL044470.
- Visser, A., A. Souza, K. Hessner, and J. Simpson (1994), The effect of stratification on tidal current profiles in a region of fresh-water influence, *Oceanol. Acta*, 17(4), 369–381.
- Wiberg, P. L., and C. R. Sherwood (2008), Calculating wave-generated bottom orbital velocities from surface-wave parameters, *Comput. Geosci.*, 34(10), 1243–1262.